FOI-R--1438--SE
November 2004
1650-1942

Scientific report

Yann Le Moigne

NFFP 542
Project report

CFD simulations of an S-duct with conventional vortex generators and comparison with experimental data

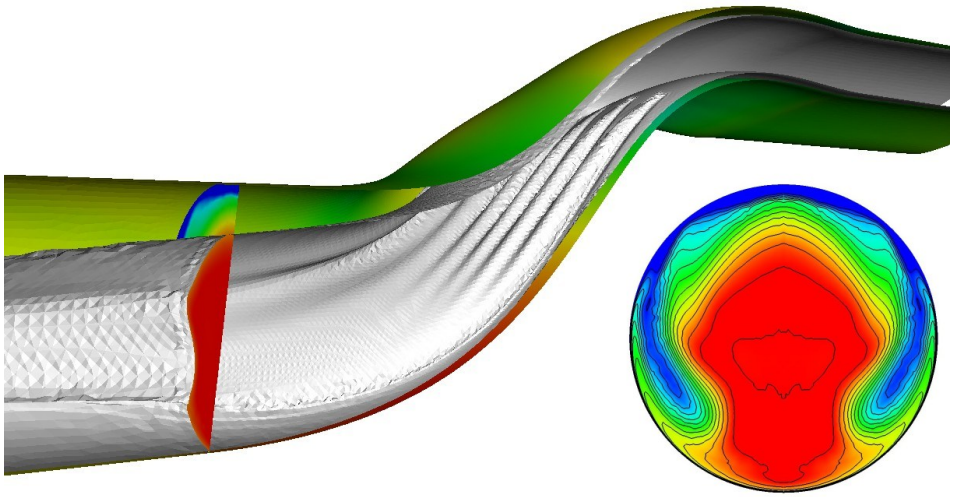

Division of Aeronautics, FFA
SE-172 90 STOCKHOLM

FOI – Swedish Defence Research Agency
Division of Aeronautics, FFA
SE-172 90 STOCKHOLM

FOI-R--1438--SE
November 2004
1650-1942

Scientific report

Yann Le Moigne

NFFP 542
Project report

CFD simulations of an S-duct with conventional vortex generators and comparison with experimental data

Division of Aeronautics, FFA
SE-172 90 STOCKHOLM

Abstract

This report presents CFD simulations of the flow in an S-duct with vortex generators (VGs) added to control the boundary layer separation. The computations are performed with the flow solver EDGE and use is made of two newly implemented boundary conditions and a VG model that makes it possible to investigate several VG configurations without remeshing.

The first part of the report deals with the comparison of experimental data and CFD results for the S-duct at several mass flow conditions, with and without VGs. The comparison is essentially made at the Aerodynamic Interface Plane (AIP) where total pressure contours are compared and the distortion indicator DC60 calculated. Overall good agreement is obtained except for the prediction of the DC60.

In the second part, an optimization of the VG configuration is performed to improve the quality of the flow at the AIP. The optimization procedure is based on the experimental design process followed by an analysis with the response surface method. An improvement of the DC60 index by 65% is achieved while the total pressure recovery remains constant.

Contents

Nomenclature

AIP	Aerodynamic Interface Plane, measurement section where the rake is located, section 2
CCF	Central Composite Face
D	Engine face diameter D = 0.180 m
DC60	Circumferential distortion descriptor for the lowest 60°-sector: DC60 = $\frac{\mathrm{P_{t2,avg}} - min(\mathrm{P_{t2}}, 60^\circ)}{\mathrm{Q_2}}$
DC60*	Quantity used to evaluate DC60: DC60 = max(DC60*), where DC60* = $\frac{\mathrm{P_{t2,avg}} - avg(\mathrm{P_{t2}}, 60^\circ)}{\mathrm{Q_2}}$
$\mathrm{D_{rad}}$	Radial distortion indicator, taken as the maximum of the radial distortion for all rings in the rake: $\mathrm{D_{rad}}$= $\mathrm{max_i}(\Delta \mathrm{PR/P_i})$= $\mathrm{max_i}\left(1 - \frac{\mathrm{P_{t,avg,i}}}{\mathrm{P_{t,avg,2}}}\right)$, where i is the ring number
h	Height of the VGs tested in the optimization phase
L	Length of the S-duct, L = 3.5D in the present case
l	Length (or chord) of the VGs tested in the optimization phase
M	Mach number
$\mathrm{N_{VG}}$	Number of vortex generators (for a whole S-duct)
P	Static pressure
$\mathrm{P_t}$	Total pressure
RECOV	Total pressure recovery at section 2: RECOV = $\frac{\mathrm{P_{t2,avg}}}{\mathrm{P_{t\infty}}}$
Q	Dynamic pressure
$\mathrm{Re_D}$	Reynolds number based on D and the mean velocity at the throat
s	Spacing between the VGs tested in the optimization phase
T	Temperature
$\mathrm{T_t}$	Total temperature
VG	Vortex generator
W	Mass flow [kg/s]
$\mathrm{W_{ac}}$	Normalized mass flow [kg/s], $\mathrm{W_{ac}} = \mathrm{W} \cdot \frac{\sqrt{\theta}}{\delta}$ with $\theta = \frac{\mathrm{T_t}}{288.15}$ and $\delta = \frac{\mathrm{P_t}}{101325}$
x,y,z	Cartesian coordinates as defined in Figure 2
δ	Boundary layer thickness

Subscript

avg	Average value
b	Bottom of the duct
cont.	Continuous value
disc.	Discrete value
e	At the exit of the duct
i	At the inlet of the duct
t	Top of the duct, also total state
∞	Free stream value
1	At section 1, the throat of the duct
2	At section 2, the AIP

1 Introduction

Newly designed low-observable UAVs and UCAVs often have S-shaped engine air intake. The two main advantages of such air-intakes are that the vehicle can be made shorter and the radar cross section of the intake is smaller than conventional pitot intake. However, the high curvature of short S-ducts leads to boundary layer separation that degrades the quality of the flow at the engine interface which ultimately causes vibration and fatigue problem for the engine compressor blades. Several means of control of the boundary layer separation have been studied and the present study focuses on conventional vortex generators (VGs).

The present Nationellt Flygtekniskt ForskningsProgram (NFFP) project 542 “Application of a vortex generator model to a typical UAV air-intake” is the continuation of the NFFP project 471 that dealt with the design of a low-observable air intake. This design is the starting point for the present project in which conventional vortex generators are used to control flow separation and thus improve the quality of the flow in the short S-duct.

The work in this CFD study is divided in two parts. At first, experimental data obtained during a rig test are compared with results of CFD computations performed on the same geometry and using a VG model to represent the real VGs of the experiment. The objective of this first part is to verify the VG model and see how CFD methods can be used to predict the effect of boundary layer control. The second part of the work makes use of the VG model to investigate several VG configurations in order to select one that gives a flow as uniform as possible at the Aerodynamic Interface Plane (AIP). This is achieved by controlling the flow separation that occurs in the duct with the VGs.

In the following, the flow solver EDGE used in the study, is first presented together with the boundary conditions and the VG model. The geometry of the S-duct is then briefly described together with the mesh generation process. Then come the two main parts of the study with first the comparison with the experimental data followed by the optimization of the VG configuration.

2 Numerical methods

2.1 The flow solver EDGE

All the simulations of the flow in the S-duct were obtained with the flow solver EDGE [1, 2], developed at the Aeronautical Division of the Swedish Defence Research Agency, FOI.
EDGE solves the Reynolds Average Navier-Stokes compressible flow equations (and Euler equations) on unstructured grids. The solver has an edge-based formulation and uses a node-centered finite volume technique to solve the governing equations. The edge-based formulation makes it possible to compute on any type of mesh: structured, unstructured (with tetrahedra, hexahedra, prisms or pyramids) or hybrid. The spatial discretization is either central with artificial dissipation or upwind; both approaches are second order accurate. For steady state computations, the time integration is explicit with the Runge-Kutta scheme. Several convergence acceleration techniques are available like agglomeration multigrid (with full multigrid capability to create a good initial solution), implicit residual smoothing and low-speed preconditioning. Time-accurate calculations are computed either explicitly with a four-stage Runge-Kutta scheme or implicitly with dual time stepping (an explicit Runge-Kutta method is used within each real time step). Several turbulence models are implemented in EDGE, including EARSM models (Explicit Algebraic Reynolds Stress Models). The program has been parallelized using the MPI message passing library and can thus be run on computers with distributed memory like Linux clusters.

The results presented in this report have been obtained with a modified version of EDGE, based on version 3.2 with the addition of new boundary conditions and a vortex generator model [3, 4]. When not otherwise indicated, the results are fully turbulent computed with the Wallin and Johansson EARSM turbulence model [5]. The computations are steady state with the central spatial discretization and 3 or 4 levels of multigrid run in full multigrid mode. The solutions require between 2000 and 3000 iterations to converge by more than 4.5 orders of magnitude (see Figure 1). The computations are typically run on 4 processors of a 72-processor HP Alpha 730MHz cluster and take between 50 and 75 hours to complete.

2.2 Boundary conditions

In order to make it easy to set the flow conditions in the simulations, three new boundary conditions have been further developed in this project and two of them adopted for the computations presented in this report. These are a mass flow boundary condition for either inlet or outlet flow and a Mach number outlet condition, see [3]. The mass flow boundary conditions are based on classical inlet (total states) and outlet (static pressure) boundary conditions, both in a weak formulation. At the inlet, the mass flow is used to calculate the total pressure corresponding to the user-specified total temperature. At the outlet, the static pressure is evaluated from the mass flow.
In order to match the mass flow of the experiment, the new outlet mass flow condition was first used, while setting the total pressure and temperature at the inlet. However, although the simulated mass flow was equal to the experimental value,

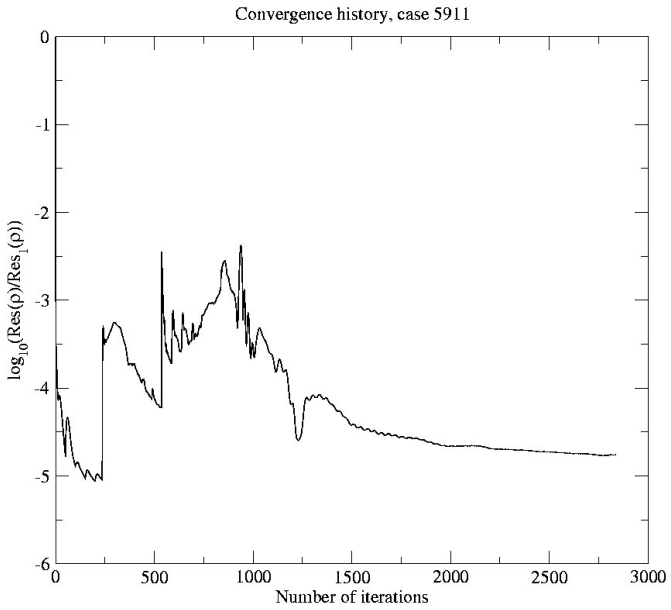

Figure 1. Typical convergence history (residuals of density, case 5911)

high Mach numbers were observed at the throat and AIP, exceeding by around 8-10% the experimentally-measured values. To solve this problem a third boundary conditions has been introduced: the outlet Mach number condition. With this boundary condition, the static pressure at the outlet is calculated from a specified Mach number. This third boundary condition is associated with the inlet mass flow condition which gives results matching both the mass flow and the throat/AIP Mach numbers within 1%. (Note that the inlet total pressure is now varying and no longer equal to the experimental value).
These three boundary conditions, recently implemented in a test version of EDGE, have been parallelized and tested on a generic test case and the last two adopted for the present simulations.

2.3 Vortex generator model

The flow conditions with vortex generators are simulated using the vortex generator (VG) model developed by Jirasek [4]. This is a numerical model that simulate the presence of VGs by adding a source term to the cells that cross the physical location of the VGs. In this way, the VGs do not have to be represented in the mesh which makes mesh generation a lot easier. In addition, a unique mesh can be used for different VG configurations or shapes, provided that the mesh is refined, with 5-8 cells in the longitudinal direction of each VG. Downstream of the VGs, the mesh should also be fine to avoid the dissipation of the vortices (see comments in section 3.2.1).

2.4 Calculation of the performance indicators

The total pressure recovery RECOV and the circumferential distortion descriptor DC60 presented in the report have been calculated in two different ways: a discrete method similar to the experimental one and a continuous approach. For the discrete method, the values of the ratio $P_{t2}/P_{t\infty}$ are extracted from the CFD results at the locations of the experimental probes. These values are then processed

in the same way as the experimental data. In the continuous approach, the average values are calculated on a whole surface (the AIP for RECOV and 60°-sectors for DC60) with the visualization software EnSight. The DC60 indicator is obtained by calculating the average total pressure on 60°-sectors covering the whole AIP in intervals of 2°.
As both approaches give slightly different results, the results with both methods are presented and refered to with the subscripts “disc.” and “cont.”.

3 Geometry and mesh generation

3.1 Geometry

The geometry of the S-duct analyzed in the present study is shown in Figures 2 and 3. The length of the duct, from the throat to the AIP, is 3.5 engine diameters D. The inlet of the duct is flat and wide in order to reduce its radar signature. The width of the inlet leads to a bend of the duct in the lateral direction in addition to the longitudinal one. Two extensions are added to the real geometry tested in the wind tunnel: one in the front, of length 2D and one at the rear, of length 3D. These two extensions are added so that the numerical boundary conditions set at the inlet and outlet do not affect the results measured at the throat and the AIP. These extensions are created by prolongating the duct horizontally both at the throat and AIP, so that the inlet and throat sections have an identical shape and the same is true for the AIP and the outlet. Only half of the duct has been modeled as shown in Figure 3, assuming a symmetrical flow field. The geometry has the same scale has the wind tunnel model i.e. the engine diameter D measures 180 mm. The AIP has thus an area of 0.0254 m^2 while at the throat the area is 0.0212 m^2, giving an area ratio between the AIP and the throat of 1.2.

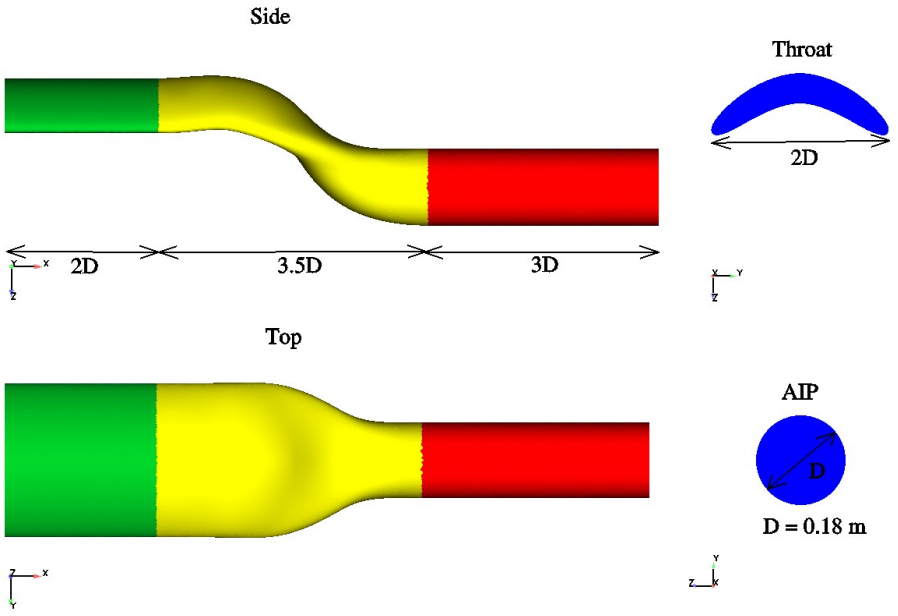

Figure 2. Geometry of the S-duct

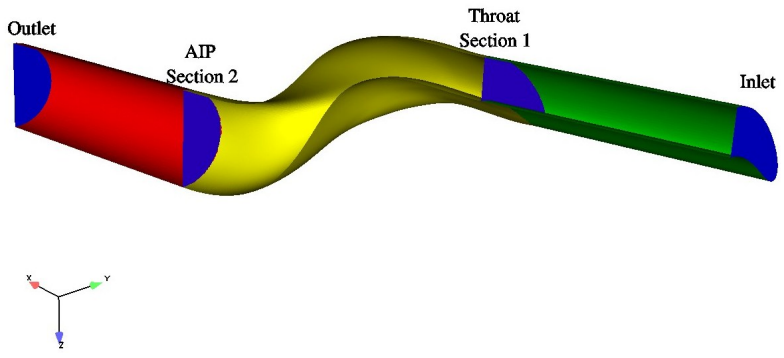

Figure 3. Perspective view of the half S-duct

3.2 Mesh generation

3.2.1 Mesh for the comparison with experimental data

Several computational meshes were generated. The final mesh selected for the computations, to be compared with the experimental data, is shown in Figure 4. The mesh has been generated with the commercial mesh generator ICEM CFD. It is a Navier-Stokes mesh with prisms in the boundary layer (40 layers with a growing factor of 1.2 and an initial height of 1.2×10^{-6} m, leading to a y^+ of less than 1) (see Figure 5). The mesh has been divided in three parts with different cell sizes: the forward part with 12 mm-cells, the rear part with 18mm-cells and the middle part (the actual S-duct) with cells measuring around 5 mm. These different regions are obtained by setting different cell sizes on the surfaces surrounding them and by using “densities” in ICEM (regions of the volume with refined cell sizes). In order to get a good accuracy with the VG model that has been used to simulate the VGs placed in the duct, the lower side of the middle region has been further refined with a cell size of only 2.5 mm. In the close-up of Figure 5,

Figure 4. Mesh of the S-duct

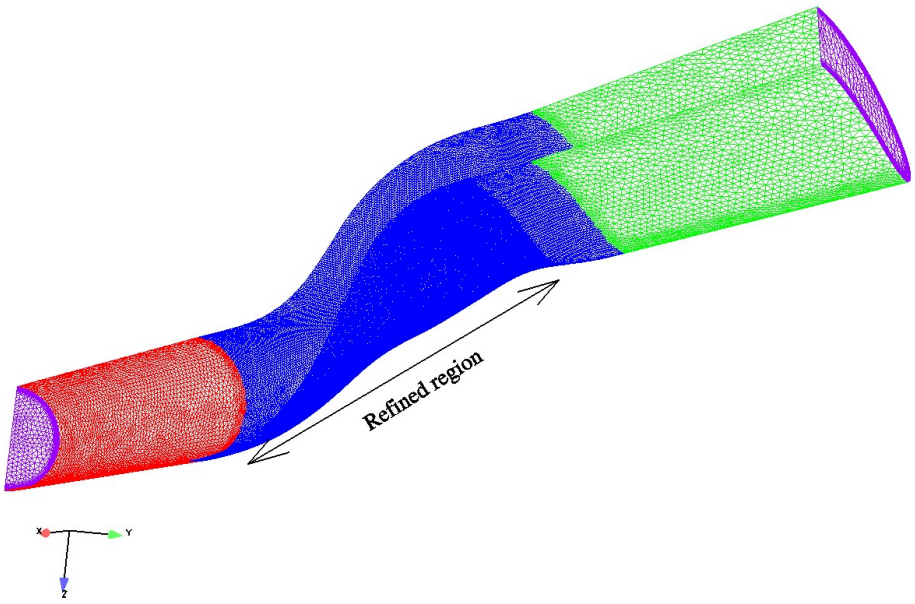

slightly upstream of the bend, the beginning of the refined region is visible on the lower side of the duct. This refined region has been extended almost to the AIP in order to capture the vortices generated at the VGs (preliminary results on a mesh with a shorter refined region showed the vortices dissipating quickly away from the refinement). The cut through the volume mesh in Figure 5 shows the prism layers and the mesh size in the volume. The resulting mesh has 4.1 million cells for 1.75 million nodes.

Figure 5. Close-up of the mesh

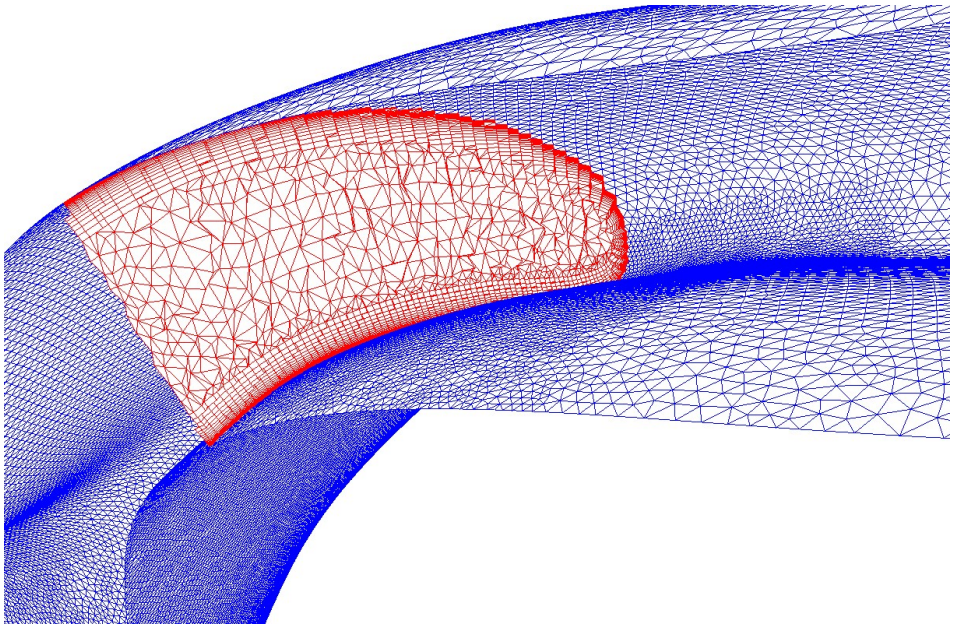

3.2.2 Mesh for the VG optimization

For the second part of the study i.e. the optimization of the VG shape and position, another mesh has been generated. In this part, VGs were placed in the corner and the upper wall of the duct which required to extend the refined region of the mesh (see Figure 6). In comparison, the refined region of the mesh used in the first part of the study stops at the corner of the duct (visible in Figure 5). Apart from the shape of the refined region, the second mesh is similar to the first one and the cell sizes are kept the same. It results in a larger number of cells, 4.65 million for 1.95 million nodes.

Figure 6. View of the refined region of the mesh used for the VG optimization

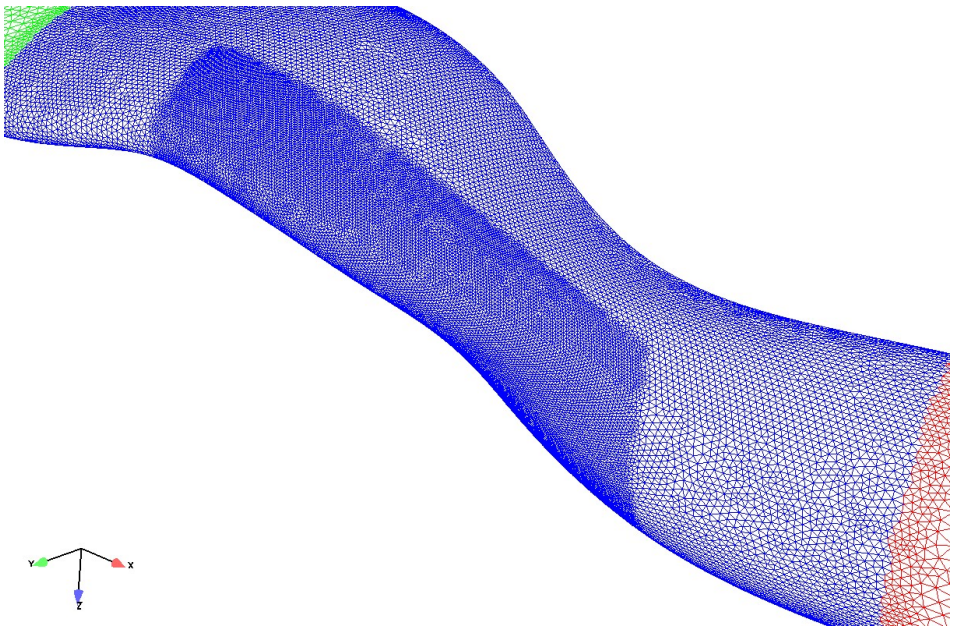

4 Flow conditions

4.1 Configurations tested

The geometry presented in the previous section corresponds to the configuration No.1 of the rig test i.e. a 3.5D long S-duct with an inlet extension of length 2D. This configuration is the one used for the calculations in a clean shape or with added VGs. The effect of the boundary layer ingestion from the inlet extension has also been analyzed by simulating the S-duct without extension (configuration No. 2). This is achieved on the same mesh by simulating the wall of the extension as a slipping (inviscid) wall.

4.2 Summary of the flow conditions simulated

A matrix of the CFD simulations performed in the first part of the study is presented in Table 1. The simulation numbers are the same as the experimental log numbers:

Table 1. Summary of the flow conditions simulated

Exp. log No.	Confi-guration	VGs	Approximate full scale mass flow	Numerical boundary conditions	
				Mass flow inlet	Mach number outlet
5909	1	–	28 kg/s	2.18 kg/s	0.480
5911	1	–	32 kg/s	2.45 kg/s	0.598
6134	2	–	32 kg/s	2.50 kg/s	0.599
5925	1	Yes	28 kg/s	2.18 kg/s	0.480
5927	1	Yes	32 kg/s	2.45 kg/s	0.598

The numerical boundary conditions are set in order to match the experimental data as close as possible. In the cases presented above, the mass flow is set by the inlet boundary condition. The Mach number at the outlet of the duct is chosen in order to yield a Mach number at the AIP close to the experimental one. And finally, the fluid viscosity is set to match the experimental Reynolds number based on the engine diameter and the velocity at the throat (estimated a priori via the mass flow). Thus the viscosity is closer to the non-standard conditions of the wind-tunnel tests (evaluation of the viscosity by the Sutherland's law to account for the non-standard temperature, yields approximately the same value as the method chosen here with the Reynolds number).

For the VG optimization part, presented in section 6, only one flow condition has been selected and it corresponds to case 5927.

5 Results and comparison with experimental data

5.1 Overview of the flow field

The flow field in the S-duct is characterized by a separation region that starts between the first and second bends (see Figures 7 and 8, the flow is from right to left, the separation is visualized as an isosurface of $P_t/P_{t\infty}$, the AIP is colored by $P_t/P_{t\infty}$ and the wall of the duct is colored by pressure). The separated region is in fact a system of two counter-rotating vortices (per half S-duct)(see Figure 9). The vortices are formed by an "overturning" flow coming from the lateral part of the duct and going towards the center, that mixes with the flow at the center of the duct (see oilflow pictures in section 5.6). Eventually, the vortices lift off after the second bend.

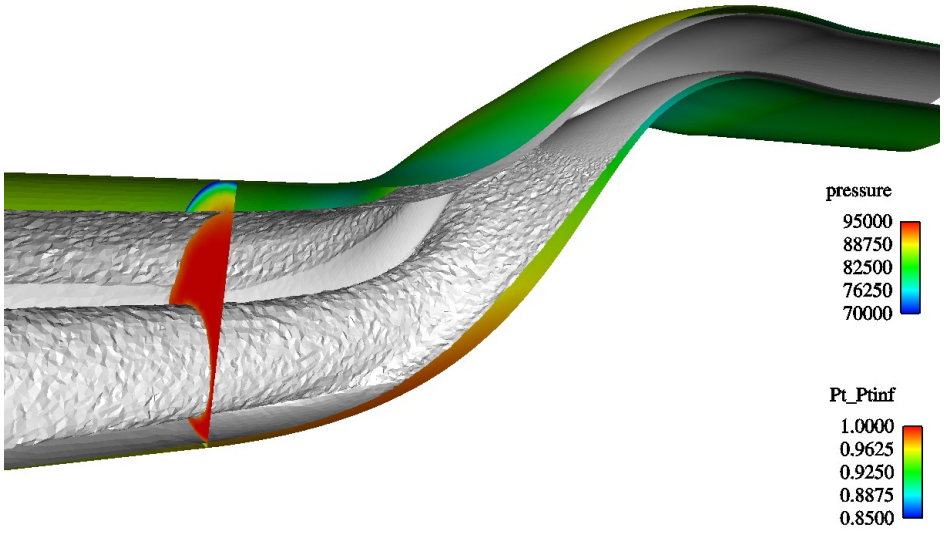

Figure 7. View of the separation region, clean configuration (case 5909)

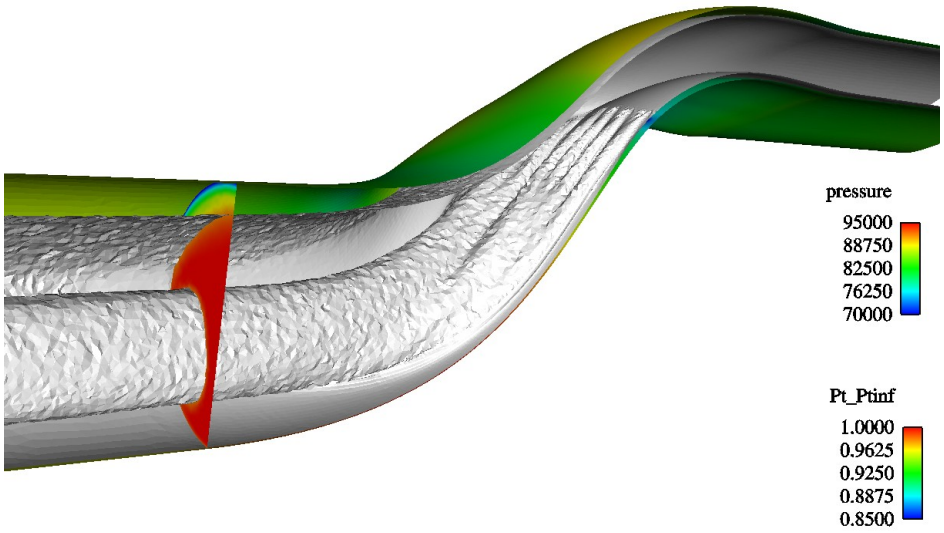

Figure 8. View of the separation region and of the vortices formed at the VGs (case 5925)

Figure 9. Countour-rotating vortices at the AIP (velocity vectors, case 5909)

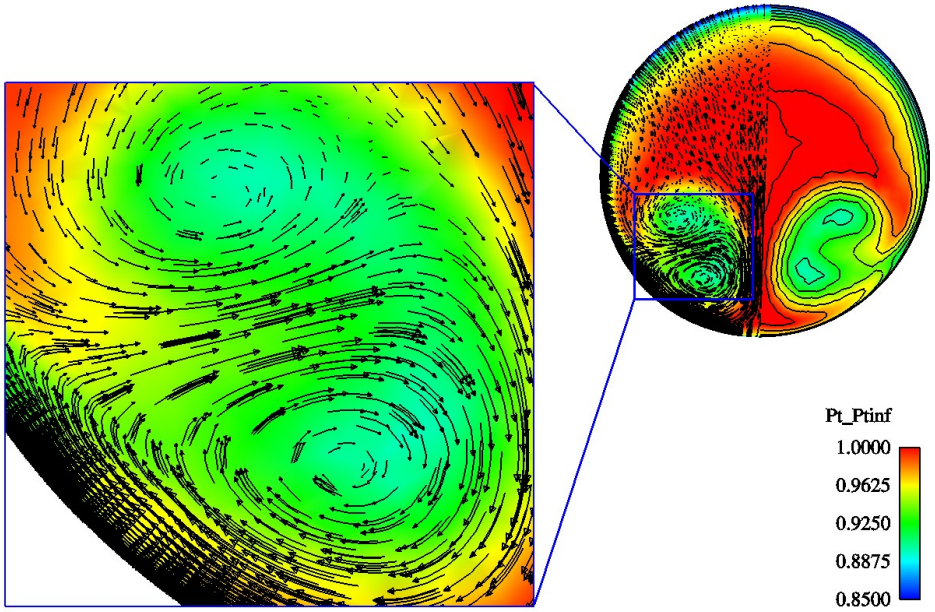

The VGs in their baseline configuration are shown in Figure 10. Note that this picture has been created for visualization purpose but the VGs are not physically present in the geometry computed, only their effect is modeled in the computations. In the baseline configuration, this effect is actually small: the VGs tend to increase the vortex lift-off and move the vortices slightly upwards. This can be seen by comparing Figures 7 and 8.

Figure 10. VG geometry for the baseline (rig test) configuration

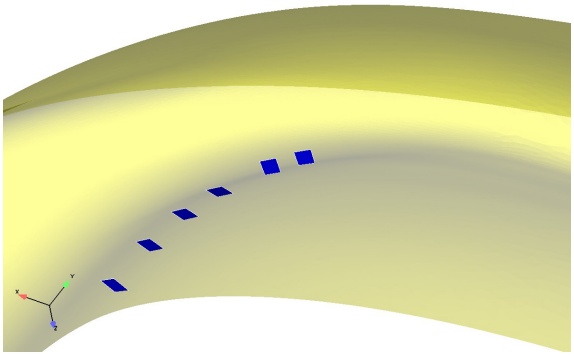

5.2 Summary of the results

An overview of the results obtained for the 5 flow conditions simulated is presented in Table 2. The results from the wind tunnel tests are included for comparison.

Case Number		5909		5911		6134		5925		5927	
		Exp.	CFD	Exp.	CFD	Exp.	CFD	Exp.	CFD	Exp.	CFD
Configuration		1	1	1	1	2	2	1	1	1	1
VGs		–	–	–	–	–	–	Yes	Yes	Yes	Yes
W_{ac2} [kg/s][1]		27.91	27.45	32.19	31.69	32.13	31.78	28.09	27.37	32.09	31.59
Re_d [10^6]		1.94	1.94	2.29	2.28	2.36	2.33	1.93	1.94	2.24	2.23
μ [10^{-5} kg/(m·s)]		–	1.90	–	1.82	–	1.82	–	1.90	–	1.86
P_{ti} [Pa]		–	105182	–	104649	–	103923	–	105673	–	105070
M_1		0.609	0.600	0.799	0.788	0.828	0.789	0.612	0.597	0.782	0.785
M_2		0.482	0.479	0.597	0.594	0.595	0.593	0.487	0.478	0.594	0.593
P_{t2} [Pa]	disc.	96778	101680	95043	98962	96527	100664	96615	102510	94826	99886
	cont.	–	101528	–	98820	–	100347	–	102308	–	99637
P_e [Pa]		–	85894	–	76491	–	77784	–	86623	–	77180
RECOV	disc.	0.9706	0.9696	0.9544	0.9457	0.9665	0.9686	0.9672	0.9701	0.9505	0.9507
	cont.	–	0.9675	–	0.944	–	0.9656	–	0.9701	–	0.9483
DC60	disc.	0.0903	0.2143	0.1005	0.2831	0.0634	0.2077	0.0988	0.1510	0.0785	0.2080
	cont.	–	0.1583	–	0.1796	–	0.1177	–	0.1356	–	0.1553
D_{rad}		0.0202	0.0262	0.0293	0.0342	0.0289	0.0391	0.0142	0.0209	0.0218	0.0300

Table 2. Summary of the results obtained and comparison with the experimental data

5.3 Results at the AIP

In this section, the distribution of the total pressure recovery at the AIP is shown with contours of $P_{t2}/P_{t\infty}$. The CFD results are compared to the experimental data and discrete CFD results.
The contours of the experimental data are obtained by interpolation. The experimental data is discrete and given at the 40 measurement points of the rake shown in Figures 11 through 15 by black dots. This data is first linearly extrapolated at the center of the AIP and at the wall for each rake. The Matlab commands are the following:

```
% Extrapolate the experimental data in the center and outer regions of AIP
center = 1E-3;
for i = 1:nrake
  exp_ratio_center(i)=interp1(ring_radius,exp_ratio(i,:),center, ...
                              'linear','extrap');
  exp_ratio_outer(i) =interp1(ring_radius,exp_ratio(i,:),R, ...
                              'linear','extrap');
end
```

The contours are then obtained by a cubic interpolation of the new experimental data on a mesh of 50×20 points. All this is done in polar coordinates:

```
interp_ratio = griddata(ring_radius,angles,exp_ratio,mesh_radius,...
                        mesh_angle,'cubic')
```

[1] Full scale value

It is important to note that the data at the center of the duct and close to the wall is extrapolated and not measured.

The contours for the “discrete” or “interpolated” CFD results are generated in the same way as for the experimental data, starting from pointwise CFD data at the location of the 40 measurement points. Here again, the data at the center of the duct and close to the wall are extrapolated.
The contours of the “continuous” CFD results are created by cutting the computational mesh at the AIP and interpolating the data from the mesh points that lie there. A lot more than 40 points are taken into account in that case so the data is close to continuous.
In general, the comparison of the experimental and the interpolated CFD contours reveals that the main features of the flow are reproduced by the simulations, However, the CFD results show a more contrasted picture of the AIP with, at the same time, higher total pressure losses in the separated and near-wall regions but also larger regions free of pressure losses. By comparing the continuous and interpolated CFD contours, it becomes obvious that taking measurements at only 40 points is too few to get an accurate picture of the flow field at the AIP. The intensity of the pressure losses and exact position of the vortices are not well predicted.

5.3.1 Effect of the mass flow

Figures 11 and 12 compare the total pressure recovery at the AIP for two cases with different mass flow: 28 kg/s and 32 kg/s. The higher losses associated with an increase of the mass flow are well reproduced by the computations.

5.3.2 Effect of the inlet extension

In Figure 13, the results for the S-duct without the inlet extension are presented. The inlet is not physically removed from the numerical mesh but it is simulated with an inviscid wall. In this way, there is no boundary layer developing on the extension wall and the conditions are close to the experimental case without extension. Comparison with the corresponding case with extension (case 5911 in Figure 12) with approximately the same mass flow, shows that eliminating the ingestion of the boundary layer from the extension reduces the total pressure losses, which is in agreement with the experimental data.

5.3.3 Effect of the VGs

The presence of the VGs has only a minor effect on the results in Figures 14 and 15 when compared to the same conditions without VGs (Figures 11 and 12 respectively). The total pressure losses are slightly lower in the vortices and their position moved upwards and away from the center, but the separation is still massive.

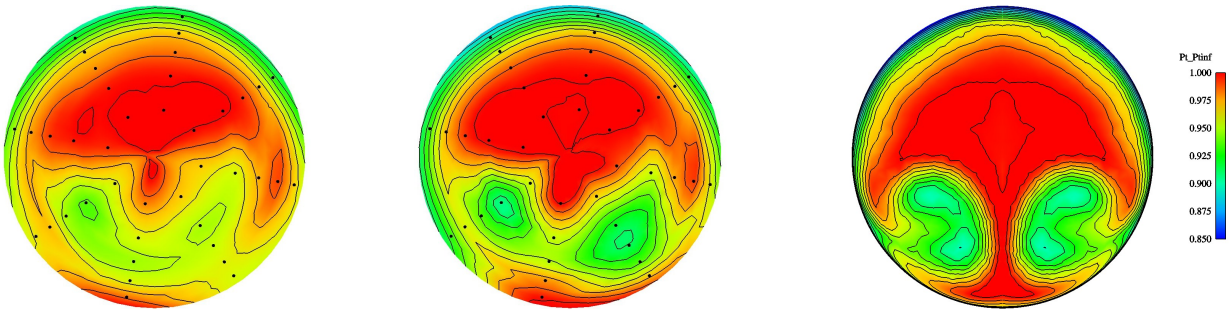

(a) Experiment (b) CFD interpolated (c) CFD

Figure 11. Contours of total pressure loss at the AIP: case 5909, W_{ac}=27.45 kg/s

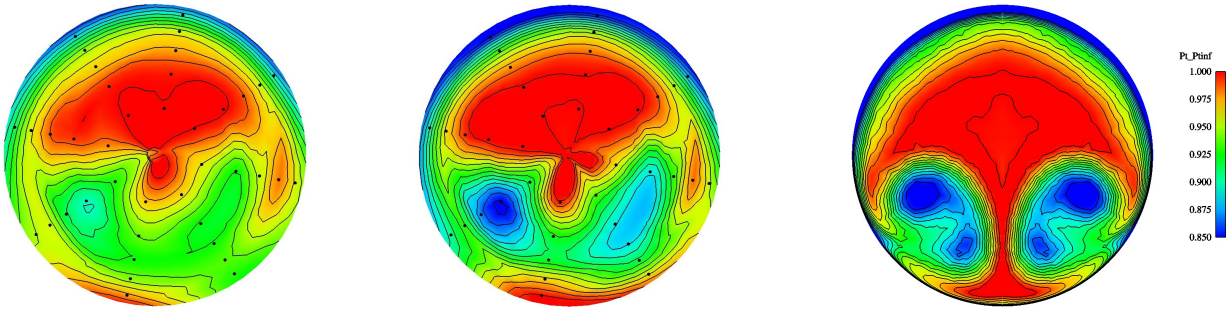

(a) Experiment (b) CFD interpolated (c) CFD

Figure 12. Contours of total pressure loss at the AIP: case 5911, W_{ac}=31.69 kg/s

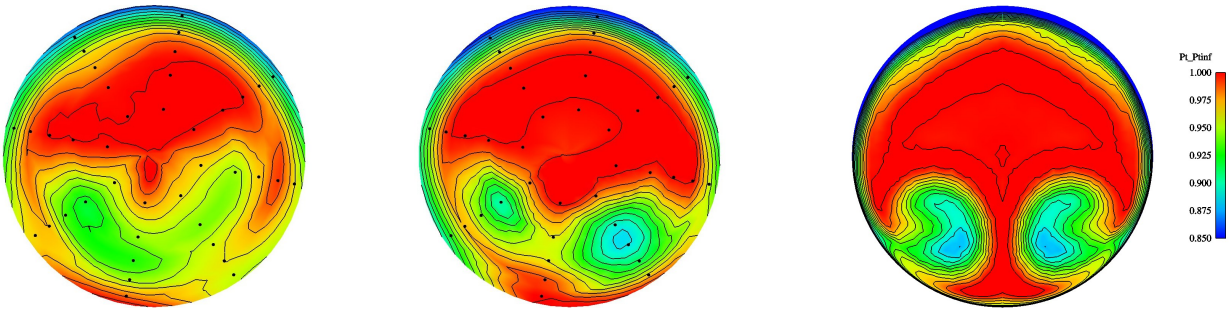

(a) Experiment (b) CFD interpolated (c) CFD

Figure 13. Contours of total pressure loss at the AIP: case 6134, W_{ac}=31.78 kg/s, no inlet extension

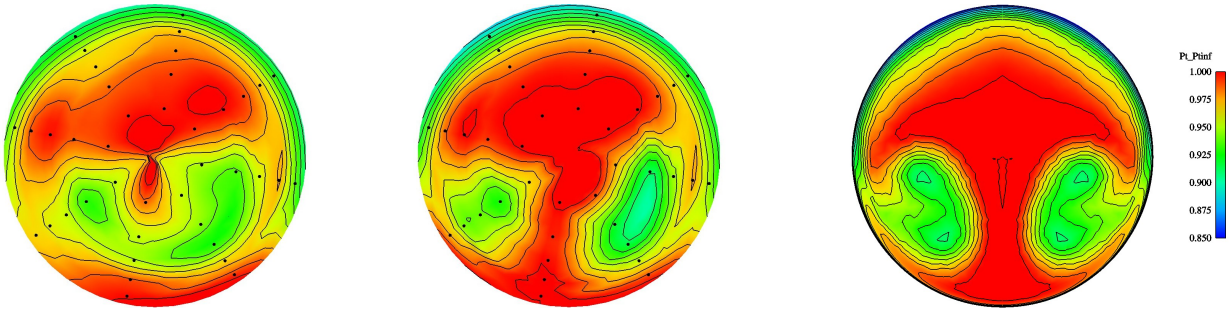

(a) Experiment (b) CFD interpolated (c) CFD

Figure 14. Contours of total pressure loss at the AIP: case 5925 with VGs, W_{ac}=27.37 kg/s

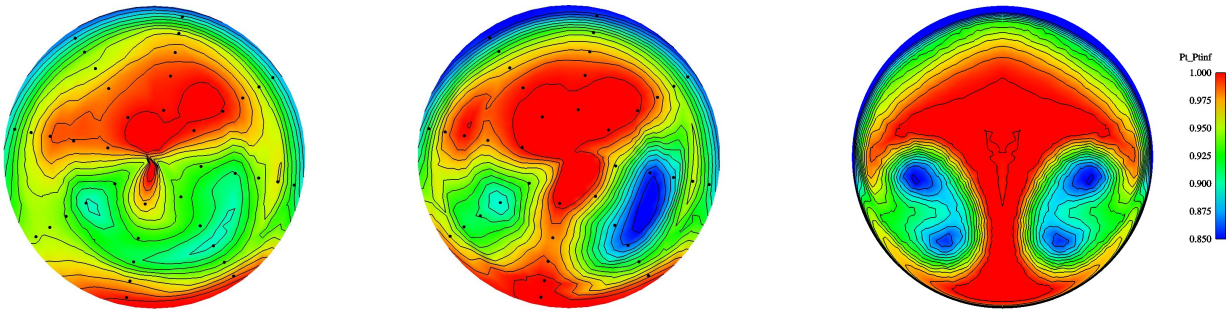

(a) Experiment (b) CFD interpolated (c) CFD

Figure 15. Contours of total pressure loss at the AIP: case 5927 with VGs, W_{ac}=31.59 kg/s

5.4 Performance indicators

5.4.1 Total pressure recovery

In Figures 16 and 17, the total pressure recovery at the AIP is compared with the experimental values for a varying mass flow and for both S-duct cases: with and without the inlet extension. As explained in section 2.4, two values are given for the CFD results, one that is continuous and the other one that is discrete, calculated in the same way as the experimental data. In this case, the two methods give values that are very close.

For both configurations, the agreement between the numerical and experimental results is quite good.[2] The decrease of the recovery as the mass flow increases is well reproduced, with almost the same magnitude as the experimental data. However, the CFD results with the VGs yield a higher recovery which is the opposite of the experimental results.

[2]The measurements of the experimental mass flows are believed to be slightly overpredicted which, if taken into account, would further improve the agreement.

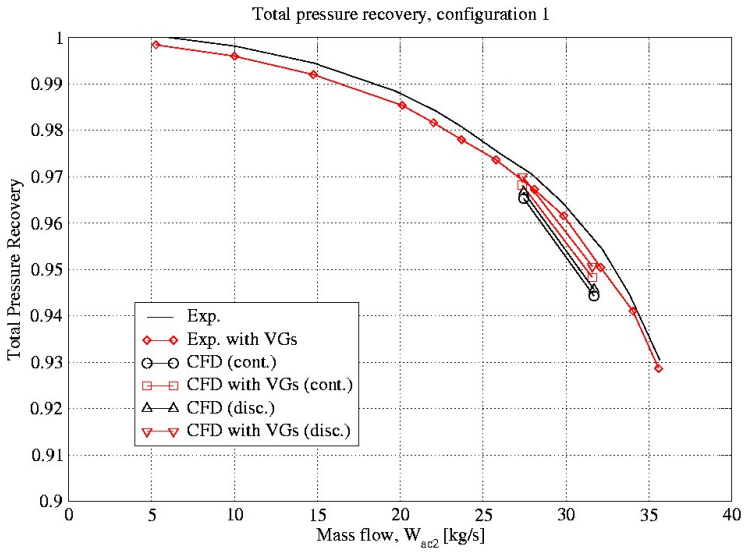

Figure 16. Total pressure recovery, configuration 1

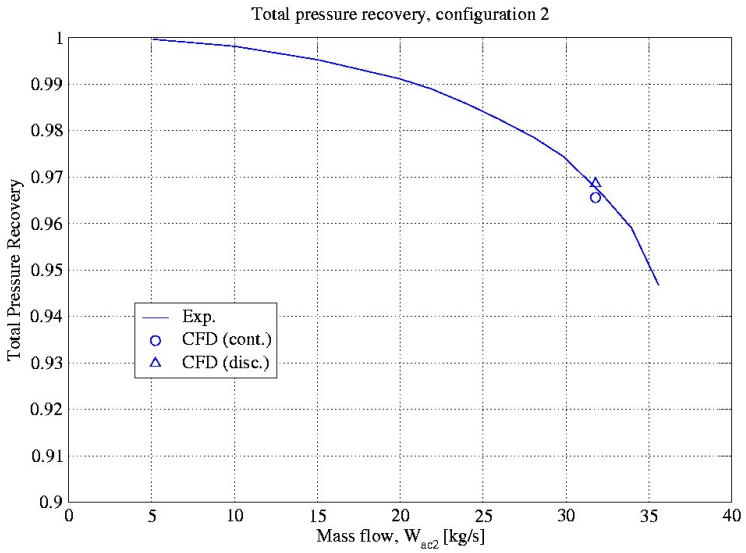

Figure 17. Total pressure recovery, configuration 2

5.4.2 Distortion indicator DC60

Figure 18 and 19 show a comparison between the experimental DC60 indicators and the one obtained with the CFD simulations. Figure 18 corresponds to the S-duct with the inlet extension while Figure 19 is for the configuration without extension. In these figures too, the continuous and discrete methods for calculating the DC60 are plotted for comparison, but this time, the difference is significant.

The CFD results are quite far from the experimental values and the agreement is even poorer when the discrete method is chosen. The differences lie between 50% and 100% which is rather large. A trend of increased DC60 with increased mass flow is observed but it is difficult to compare that with the experiment. The CFD results of the configuration with the VGs tend to show that the VGs decrease the distortion at the AIP.

On the other hand, the experimental DC60 are also difficult to analyze. No improvement is observed with the VGs. The curves are not smooth and make it difficult to identify any trend, indicating a very sensitive result.

Figure 18. Distortion indicator DC60, configuration 1

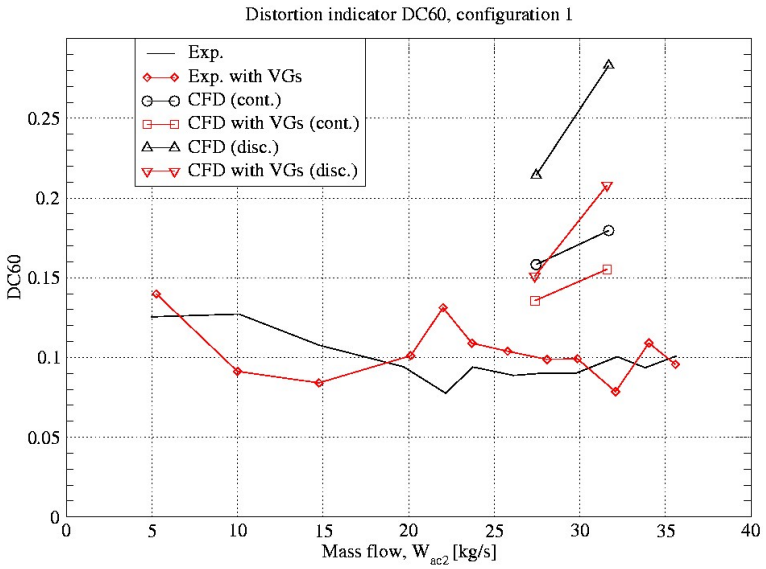

Figure 19. Distortion indicator DC60, configuration 2

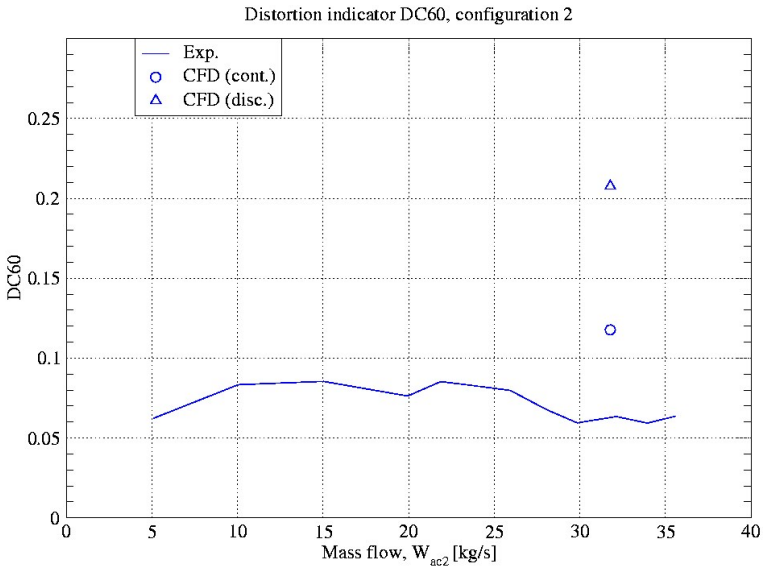

5.4.3 Radial distortion indicator D_{rad}

D_{rad} gives an indication of the distortion in the radial direction. It is a discrete quantity calculated as the maximum of the average total pressure loss for each ring. In the cases without VGs, this maximum is usually found at the outer ring, close to the wall. The comparison of the "interpolated" CFD D_{rad} with the experimental D_{rad} is shown in Figures 20 and 21. In this case too, the CFD results predict higher losses than the experiment.
(Note that D_{rad} is a discrete quantity).

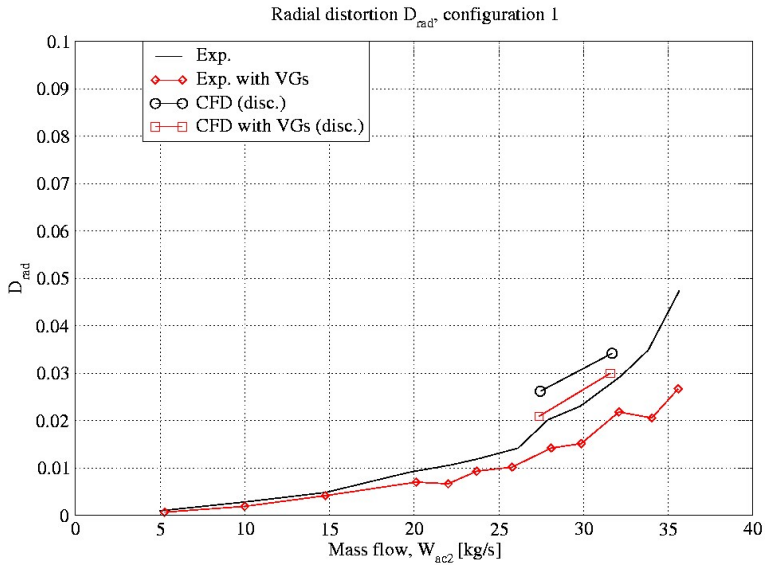

Figure 20. Radial distortion indicator D_{rad}, configuration 1

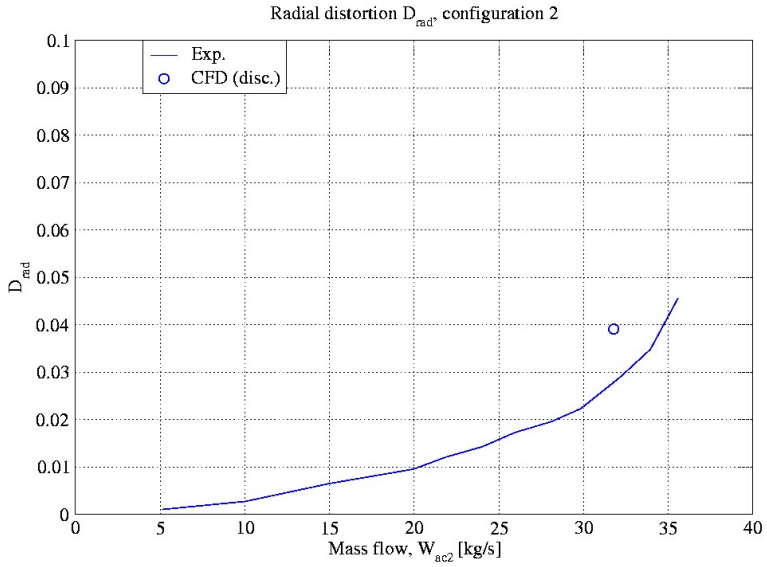

Figure 21. Radial distortion indicator D_{rad}, configuration 2

5.5 Pressures on the wall

An overview of the pressure distribution on the wall of the S-duct is presented in Figures 22 and 23, for the clean configuration and the one with VGs. The classical pressure distribution for S-ducts can be seen with high pressure regions downstream of the bends and corresponding low pressure regions in the bends. A low pressure region is noticeable downstream of the throat on the top wall. It is due to a very small bump just aft of the throat. In Figure 23, the trace of the vortex generators are visible.

Figures 24 through 28 show the comparison of the pressure distribution on the wall in the plane of symmetry between the CFD results and the experimental measurements. The pressure is measured between the throat (“0” on the x-axis) and the AIP (“1” on the x-axis).

The agreement between the CFD and experimental results is in general rather poor. For the top wall, the increase of pressure in the first bend and the decrease

Figure 22. Pressure distribution on the wall, case 5909

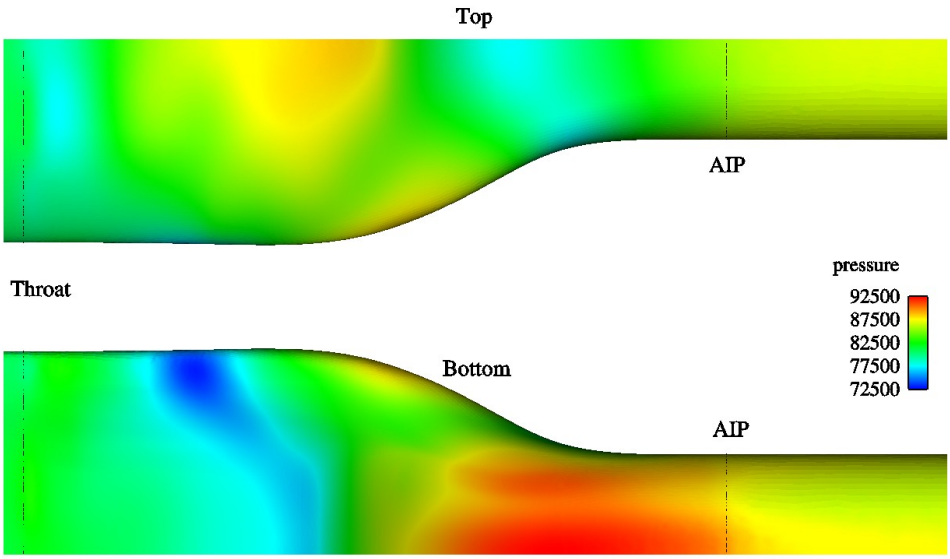

Figure 23. Pressure distribution on the wall, case 5925 with VGs

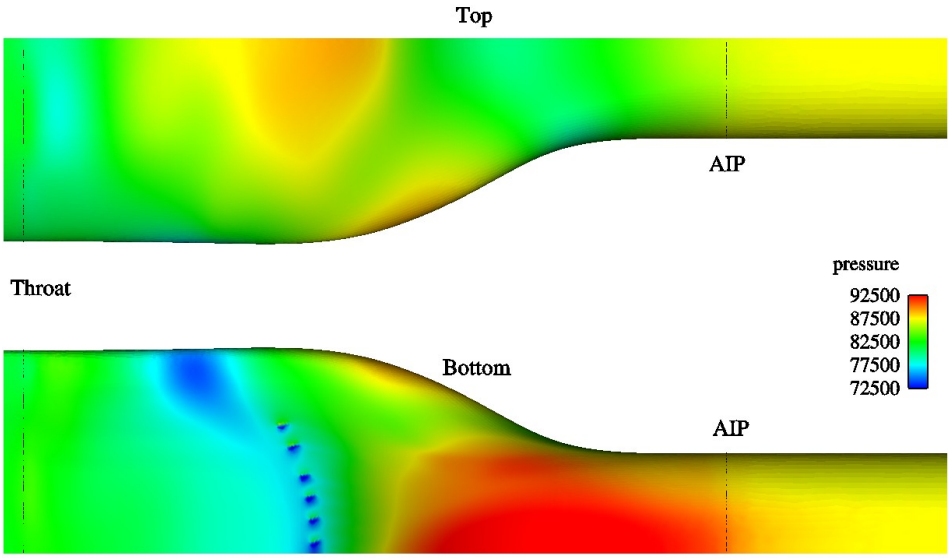

in the second bend are predicted but further downstream. One more measurement point just aft of the throat would be interesting to see if the predicted region of low pressure due to the bump (see above) is present in the experiment. The prediction of the pressure distribution on the bottom wall is more contrasted than the experimental measurements: in some of the experimental data, the region of low pressure in the first bend is missing and only a slow increase in pressure is present whereas the low pressure region is always predicted by CFD.

5.5.1 Effect of the mass flow

Figures 24 and 25 show the effect of an increase in mass flow. The difference between the CFD and the experimental results is larger for a higher mass flow. The pressure drop on the bottom wall at the first bend is not measured experimentally

for these two conditions but appears in the cases presented below.

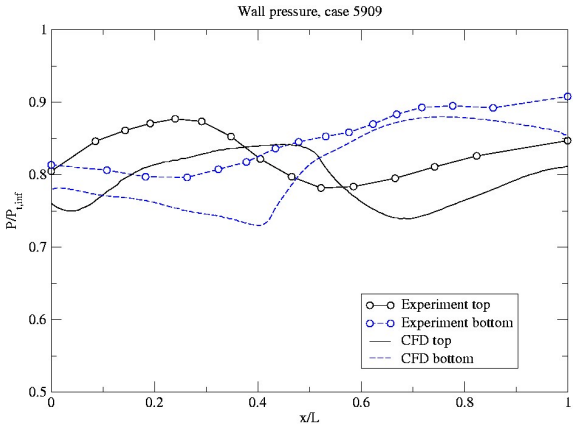

Figure 24. Pressure distribution on the wall: case 5909

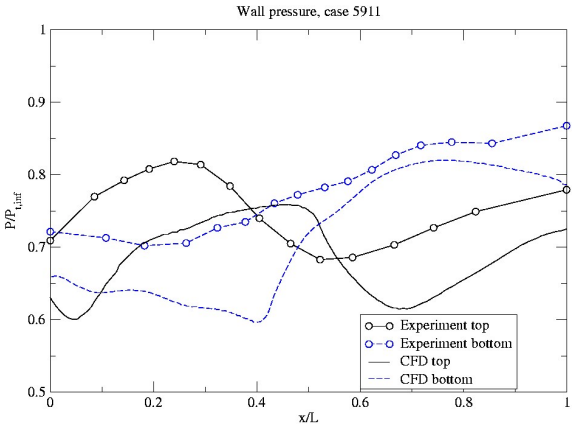

Figure 25. Pressure distribution on the wall: case 5911

5.5.2 Effect of the inlet extension

The pressure distribution for the S-duct without the inlet extension in Figure 26 is very similar to the one for the configuration with the extension in Figure 25, the pressures beeing only slightly lower in the latter case. The experimental measurements however are a bit different with the pressure tap at x/L = 0.35 showing a pressure drop in the first bend, in agreement with the CFD data.

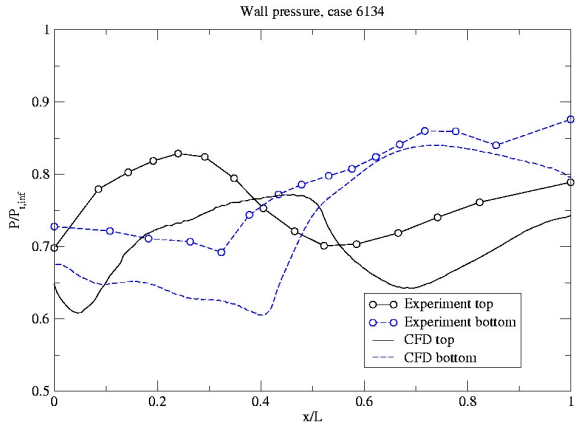

Figure 26. Pressure distribution on the wall: case 6134

5.5.3 Effect of the VGs

The effect of the VGs on the experimental pressure distribution is small and limited to the region close to them. In Figure 27 and 28, the difference is seen for the pressure taps between x/L = 0.3 and 0.4 with a drop of pressure not seen in Figures 24 snd 25 for the configurations without VGs. Concerning the CFD pressure distribution, the main differences lies at the same location, x/L = 0.4, where

the dip in the pressure is more pronounced. This is due to the presence of the two VGs on each side of the middle plane that affect the flow locally.

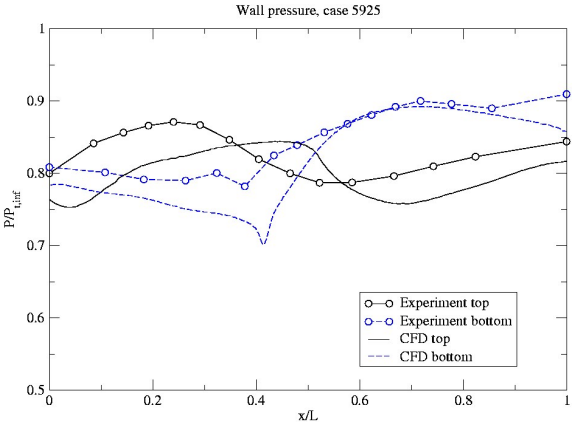

Figure 27. Pressure distribution on the wall: case 5925 with VGs

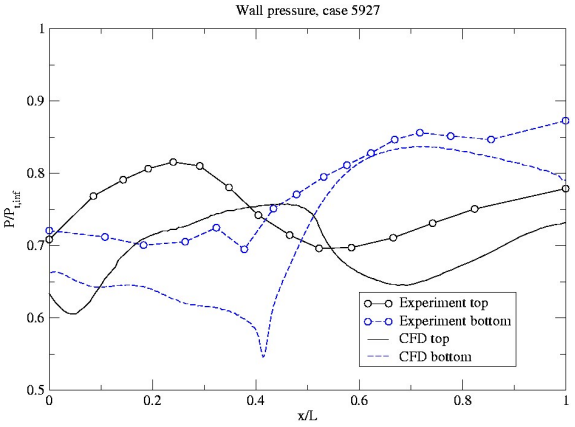

Figure 28. Pressure distribution on the wall: case 5927 with VGs

5.6 Oilflow visualization

Figures 29 and 30 show streamline visualization close to the wall of the S-duct, so-called oilflow visualization in reference to the experimental visualization technique. The most interesting view is from below, where the streamlines spiral into a focus, characteristic of the foot of a vortex that lifts-off from the surface. The overturning of the flow from the side is also visible and help explain the formation of the vortex.

Figure 29. Case 5909 (no VG)

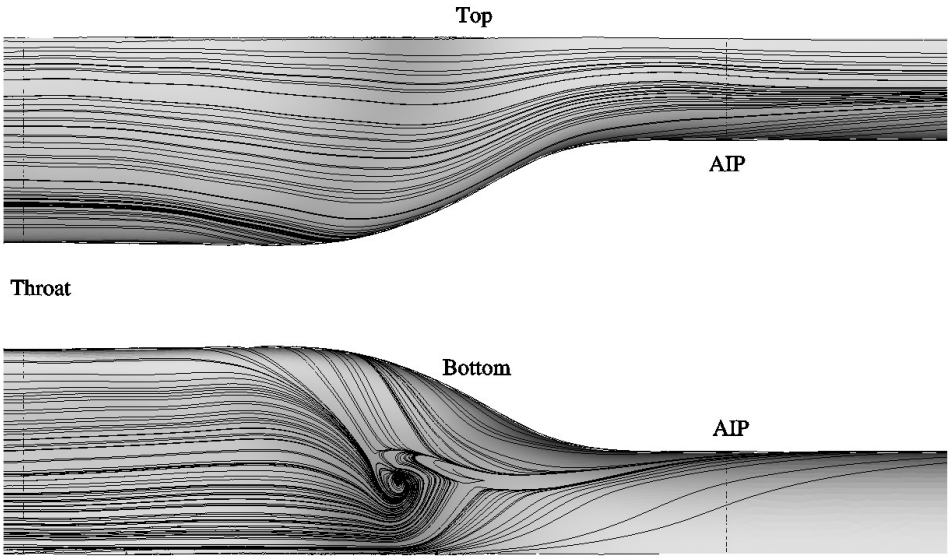

In Figure 30, the effect of the VGs is visible, with streamlines that turn away from the center of the duct. In that case, the streamlines are less rotating but that does not prevent the formation of the focus.

Figure 30. Case 5925 (with VGs)

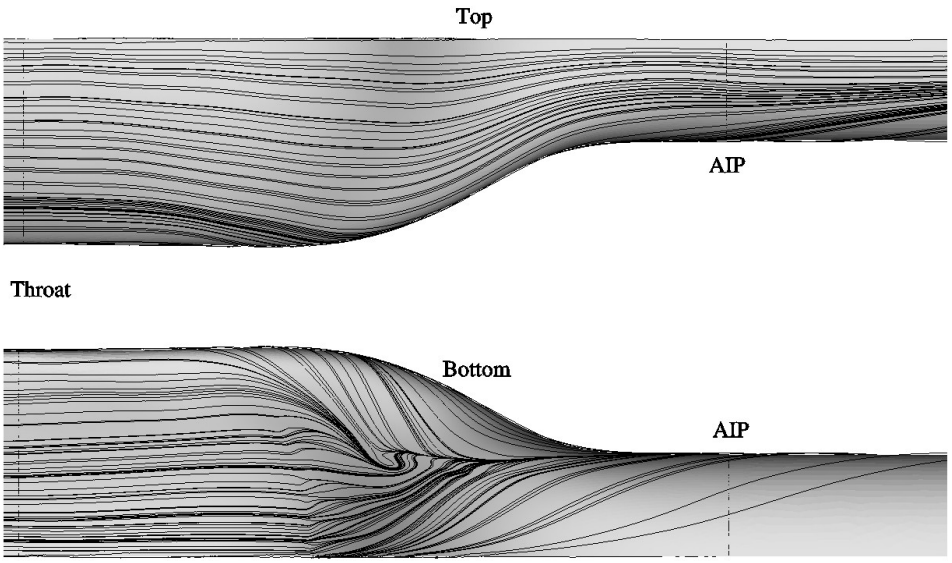

5.7 Skin friction visualization

Figures 31 and 32 show the skin friction coefficient distribution on the wall. Regions of skin friction close to zero indicate that the flow is separated. The comparison of the two figures reveals that the VGs do not prevent the massive separation, except close to the symmetry plane. Figure 32 also shows that more VGs are needed in the corner, at the outer region of the first bend where the separation begins.

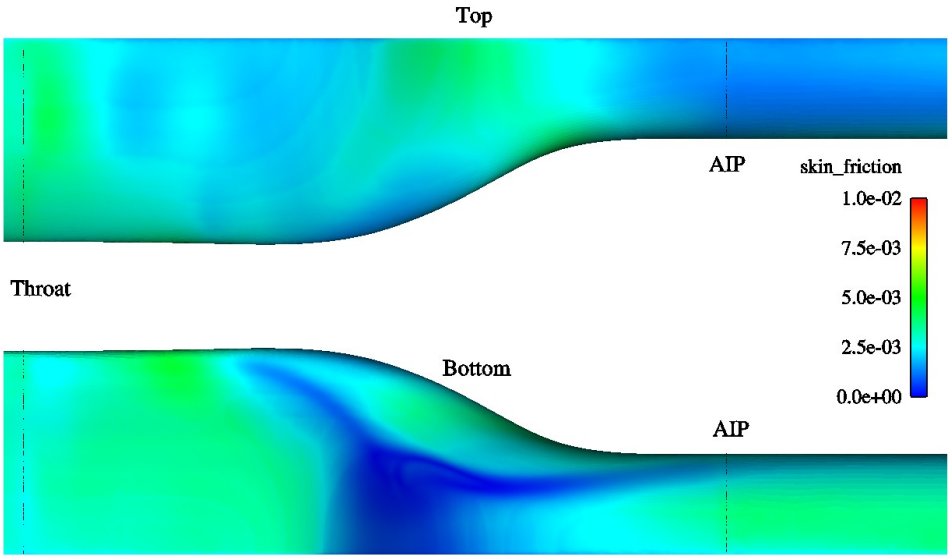

Figure 31. Skin friction, case 5909 (no VG)

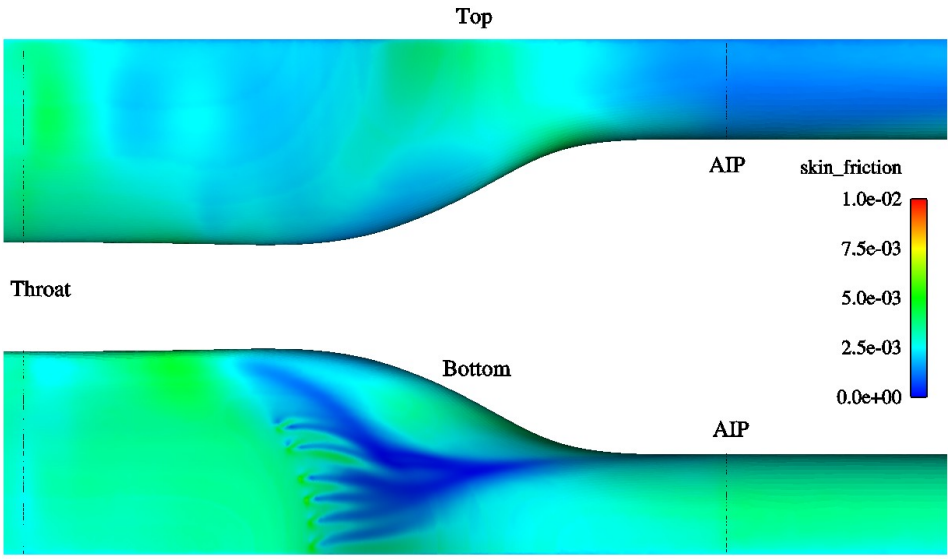

Figure 32. Skin friction, case 5925 (with VGs)

6 Optimization of the VG configuration

In this part, the results of an optimization of the VG shape and position are presented. The aim of the exercise is to find a VG configuration that, if possible, both minimizes the DC60 indicator and maximizes the total pressure recovery at the AIP. The flow conditions chosen correspond to case No 5927 with a corrected mass flow W_{ac} of around 32 kg/s. In this study, only conventional VGs with a height larger than 50% of the boundary layer thickness are considered.

6.1 Methodology

6.1.1 Experimental design

In order to find an optimum VG configuration, a parametric study following the principles of the experimental design [6] has been carried out. The experimental design is a scientific approach used to get knowledge about a system. In the present study, the purpose is to understand how the shape and position of the VGs (inputs) affect the flow in the S-duct and in particular the total pressure recovery and the DC60 indicator (outputs). In addition, by following the experimental design methodology, several parameters like the height and length of the VGs can vary at the same time and the coupling of these parameters identified. Using the knowledge of the effect of each parameter on the flow in the S-duct, an optimum configuration can be designed using a surface response method.

6.1.2 Optimization set-up

Due to the expected non-linearity of the problem, each parameter has to be tested for three different values. Only three different parameters were at first considered due to budget and time constraints. Using a full factorial design where all the parameters take the three possible values would require computing 3^3=27 configurations. Following the guidelines in [6], the design finally chosen is a Central Composite Face (CCF) design which necessitates only 15 computations and is the most efficient second-order modeling design for quantitative parameters as is the case here.

The three parameters chosen for the optimization are the height (h) of the VGs, their length (l) (or chord) and the spacing (s) between them. These parameters are defined in Figure 33. Other possible parameters like the x-position of the VGs ("X" in Figure 33) or their angle of attack ("α" in Figure 33) were kept constant in this study: X = 250 mm from the throat and α=22°. Figure 34 gives an idea of the position of the VGs in the S-duct. Note that some VGs are placed in the corner of the duct and on the upper wall.

The boundary layer thickness δ at this x-location has been estimated to 8 mm. Based on this value, the height of the VGs (h) has been varied between 6 and 10 mm (75%-125% of δ), the length (l) between 14 and 26 mm and the spacing (s) between 18 and 30 mm (see Table 3). The spacing s influences the number of vortex generators in the configuration since the position of the outermost VG has been kept approximately constant. A spacing of 18 mm corresponds to 28 VGs in the S-duct, 24 mm to 22 VGs and for a spacing of 30 mm only 18 VGs are used.

Figure 33. Definition of the parameters chosen for the optimization

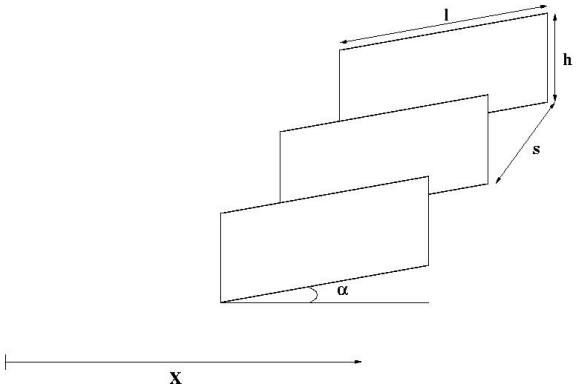

Figure 34. View of the position of the VGs in the duct, configuration 13

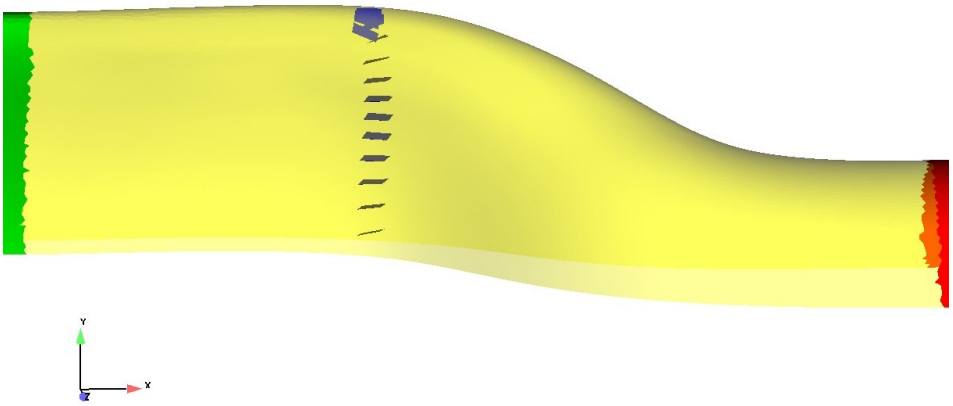

The 15 configurations tested in the CCF design can be presented in a cube as shown in Figure 35. The three axes of the cube represent the three parameters h, l and s that can take each 3 different values. The blue corner points are used to understand the linear effect of the parameters while the green middle point and the red face-center points are used to assess the non-linear effects.

Figure 35. Representation of the 15 configurations of the CCF design

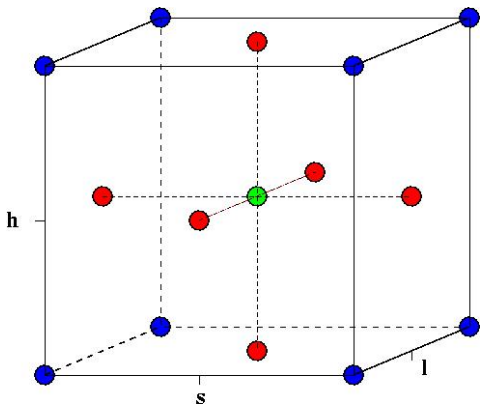

In Table 3, all the configurations tested are presented. The 8 first configurations are the corner points, the ninth is the middle point and configurations 10-15 are the face centers. The last four configurations in Table 3 are additional configurations presented in section 6.4. The first 4 columns in Table 3 show the parameter settings, followed by h/δ, the relative length and spacing in columns 5, 6 and 7. The number of VGs is also given. The columns at the right are the results obtained, calculated both with the continuous and the discrete methods (see section 2.4) and

presented in more details in the next section. Note that the “Baseline” case in the first row corresponds to the S-duct without any VG but with the same flow conditions (numerical boundary conditions) as case 5927 that has been chosen for the optimization.

Conf. No	h [mm]	l [mm]	s [mm]	$\frac{h}{\delta}$	$\frac{l}{h}$	$\frac{s}{h}$	N_{VG}	$RECOV_{cont.}$	$DC60_{cont.}$	D_{rad}	$RECOV_{disc.}$	$DC60_{disc.}$
Baseline	–	–	–	–	–	–	–	0.9444	0.1704	0.0350	0.9466	0.2720
1	6	14	18	0.75	2.33	3.00	28	0.9498	0.1299	0.0405	0.9524	0.1428
2	6	26	18	0.75	4.33	3.00	28	0.9471	0.1832	0.0401	0.9497	0.2169
3	6	14	30	0.75	2.33	5.00	18	0.9500	0.0891	0.0502	0.9519	0.1054
4	6	26	30	0.75	4.33	5.00	18	0.9482	0.1627	0.0423	0.9505	0.1643
5	10	14	18	1.25	1.40	1.80	28	0.9478	0.1916	0.0368	0.9505	0.1939
6	10	26	18	1.25	2.60	1.80	28	0.9447	0.2635	0.0286	0.9481	0.2605
7	10	14	30	1.25	1.40	3.00	18	0.9474	0.1403	0.0325	0.9496	0.1950
8	10	26	30	1.25	2.60	3.00	18	0.9447	0.2667	0.0276	0.9466	0.3006
9	8	20	24	1.00	2.50	3.00	22	0.9484	0.1837	0.0329	0.9510	0.1822
10	10	20	24	1.25	2.00	2.40	22	0.9465	0.2020	0.0280	0.9491	0.2158
11	6	20	24	0.75	3.33	4.00	22	0.9490	0.1406	0.0425	0.9509	0.1399
12	8	20	30	1.00	2.50	3.75	18	0.9470	0.1586	0.0373	0.9492	0.1504
13	8	20	18	1.00	2.50	2.25	28	0.9467	0.2113	0.0350	0.9497	0.2170
14	8	26	24	1.00	3.25	3.00	22	0.9462	0.2198	0.0284	0.9486	0.2187
15	8	14	24	1.00	1.75	3.00	22	0.9487	0.1334	0.0358	0.9511	0.1342
3a	6	14	30	0.75	2.33	5.00	14	0.9507	0.1093	0.0505	0.9526	0.1319
3b	6	14	30	0.75	2.33	5.00	10	0.9503	0.1178	0.0595	0.9523	0.1624
16	4	9	30	0.50	2.25	7.50	18	0.9488	0.0812	0.0518	0.9508	0.1278
17	4	9	18	0.50	2.25	4.50	28	0.9494	0.0602	0.0478	0.9515	0.0822

Table 3. Geometry of the VG configurations and results obtained

In Figure 36, three VG configurations are shown as examples. Configuration 3 has the smallest VGs, configuration 8 the largest and in configuration 13 intermediate VGs are used. In the three pictures, the spacing is also different.

6.2 Results

In this section, the results of the computations performed on the 15 configurations presented above are briefly described. The results in the form of DC60 indicator and total pressure recovery at the AIP have already been shown in Table 3. The DC60 varies strongly from 0.09 (configuration 3) to more than 0.26 (configuration 8) while the total pressure recovery is almost constant between 0.945 and 0.950.

Figure 37 shows how the separation is modified by the VGs in configurations 3 and 8 compared to the baseline case. The results with configurations 3 and 8 are chosen as examples because they are quite different from the baseline. The baseline case (Figure 37(a)) is very similar to case 5909 previously shown in Figure 7 with a system of counter-rotating vortices in the bottom-half of the AIP. The vortices created by the VGs in configuration 3 (Figure 37(b)) tend to minimize the separation and contain it closer to the side-wall. However, in this case the flow is more separated on the upper wall. In Figure 37(c), we see that the vortices in the bottom of the S-duct are less developed but another system of vortices has

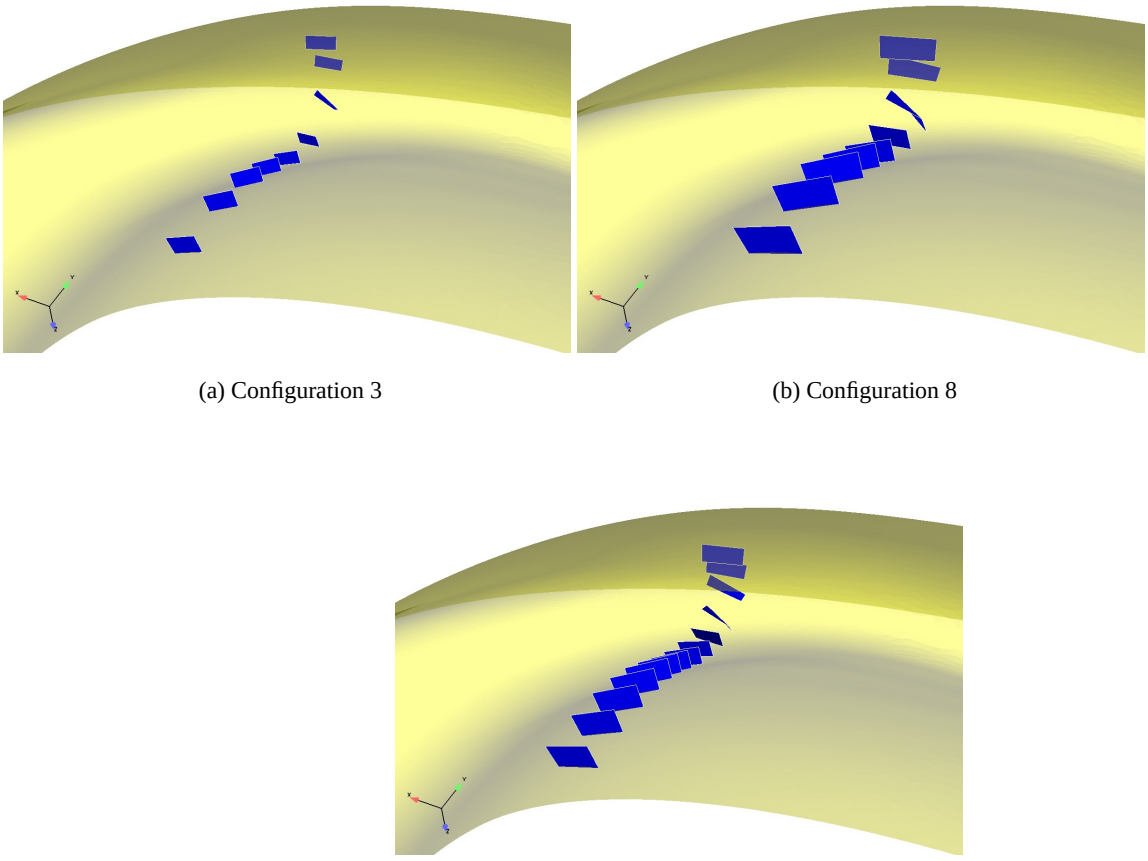

(a) Configuration 3

(b) Configuration 8

(c) Configuration 13

Figure 36. Examples of VG geometries

formed close to the top wall, which yields the poor DC60 results for configuration 8. Compared to the configuration used in the rig tests (see Figure 8 for example), the new VG configurations have clearly more effect on the flow field and really affect the separation in the duct.

This is even more visible in the contours of total pressure losses in Figure 38. The results for configurations 3 and 8 are clearly different from the baseline, much more than what has been shown in Figure 15(c) for the rig-test configuration. The good DC60 results of configuration 3 are explained by a more uniform distribution of the pressure losses all around the AIP, leading to a more uniform flow. On the contrary, in Figure 38(c), the losses are concentrated in the top part of the AIP, leading to a poor DC60. For the three cases shown in Figure 38, the total amount of pressure losses at the AIP is approximately the same which gives only small changes in the total pressure recovery.

Figure 39 shows a comparison of the circumferential distribution of $DC60^*$ for the baseline and configurations 3 and 8. θ is the circular angle oriented clockwise with zero at 12 o'clock. In such a graph, it is easy to see which part of the flow

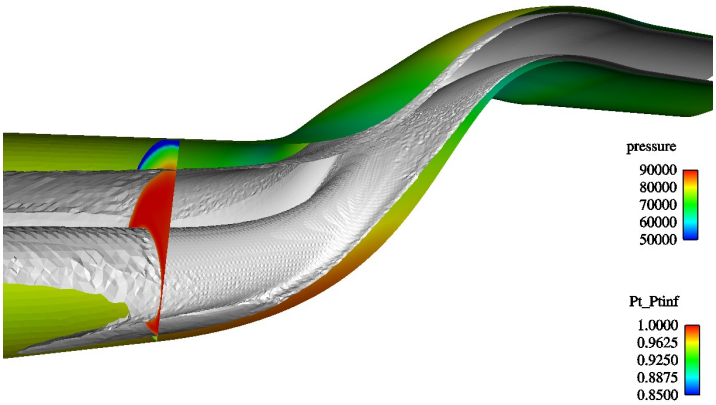

(a) Baseline

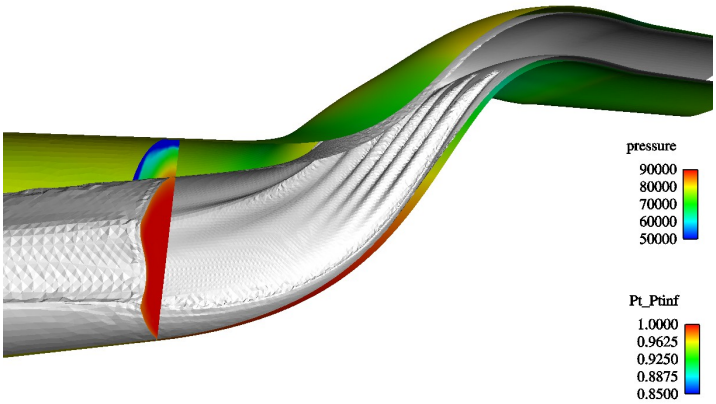

(b) Configuration 3

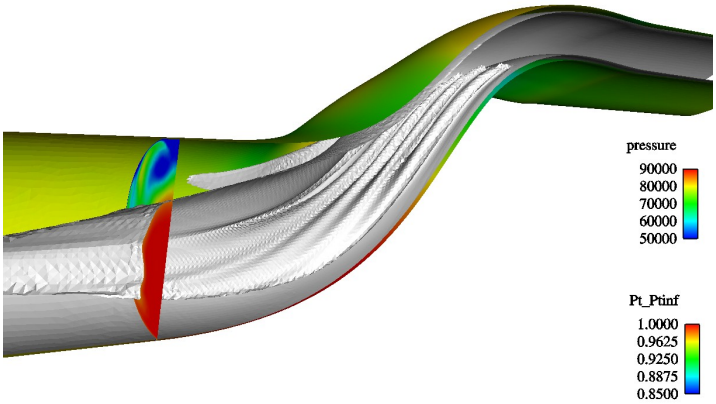

(c) Configuration 8

Figure 37. View of the separation for three configurations

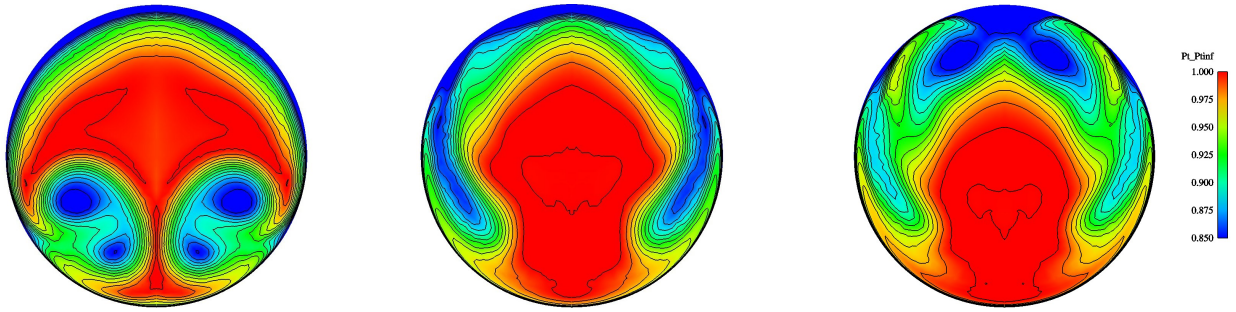

(a) Baseline (b) Configuration 3 (c) Configuration 8

Figure 38. Contours of total pressure loss at the AIP for three configurations

contributes to a high DC60 value: the high distortion for the baseline is due to the two vortices in the lower part; for configuration 3, the losses are almost constant until θ reaches 110°, while for configuration 8, the higher distortion is reached in the top part. Again Figure 39 witnesses that the VGs have a strong effect on the flow at the AIP and have the potential to reduce the distortion there.

Figure 39. Circumferential distribution of DC60*

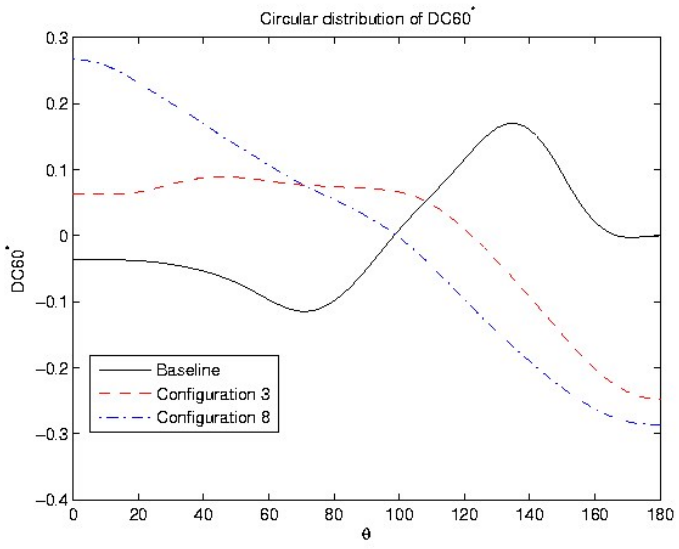

In Figure 40, the skin friction coefficient is compared for the baseline and configurations 3 and 8. The regions of low friction in the baseline case, show how the flow first separates in the outer part of the duct before the whole middle region experiences separation too. With the VGs in configuration 3 (Figure 40(b)), the separation region is altered and moves to the side of the AIP. In configuration 8, the separation is moved even more and reaches the top of the duct, although it is difficult to clearly see a difference with configuration 3 in this picture.

Figure 41 shows how the VGs modify the streamlines close to the wall of the duct. The oilflow visualization for the baseline configuration is very similar to

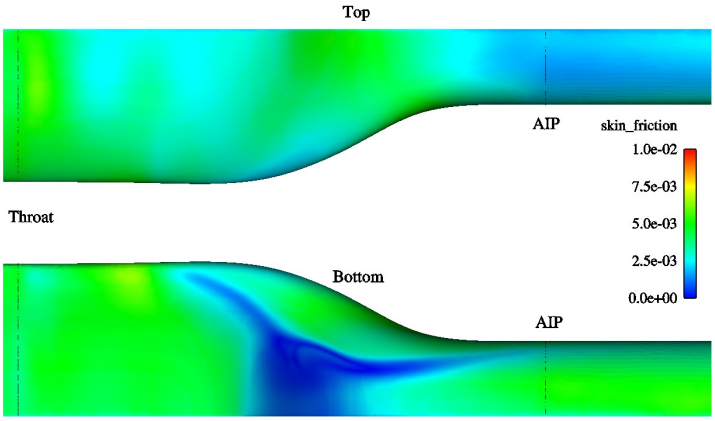

(a) Baseline

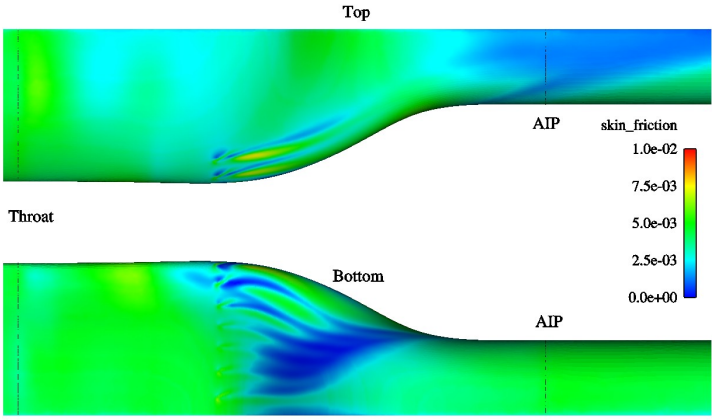

(b) Configuration 3

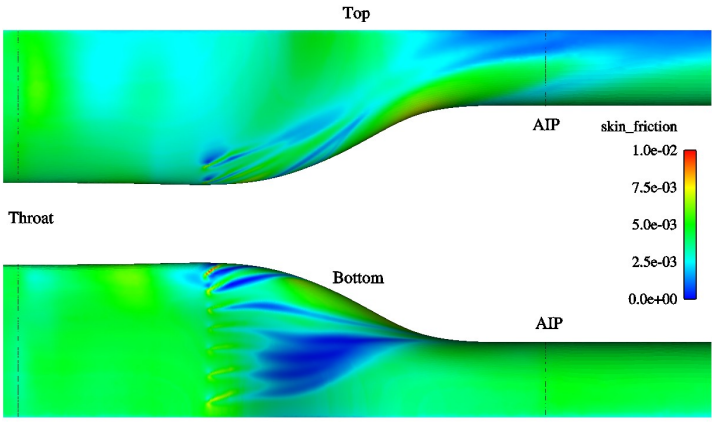

(c) Configuration 8

Figure 40. Skin friction visualization for three configurations

case 5909 in Figure 29 and is therefore not reproduced here. In Figure 41(a), we see how the VGs in the outer part of the bottom wall prevent the overturning of the flow in the first bend and thus reduce the separation and formation of a strong vortex system. In configuration 8 (Figure 41(b)), the VGs have a stronger effect (certainly due to their larger size) and the flow is now turning in the other direction. The change in the flow direction is even too large as can be seen on the top view of Figure 41(b): the flow close to the wall now comes too much towards the center of the S-duct and vortices form there.

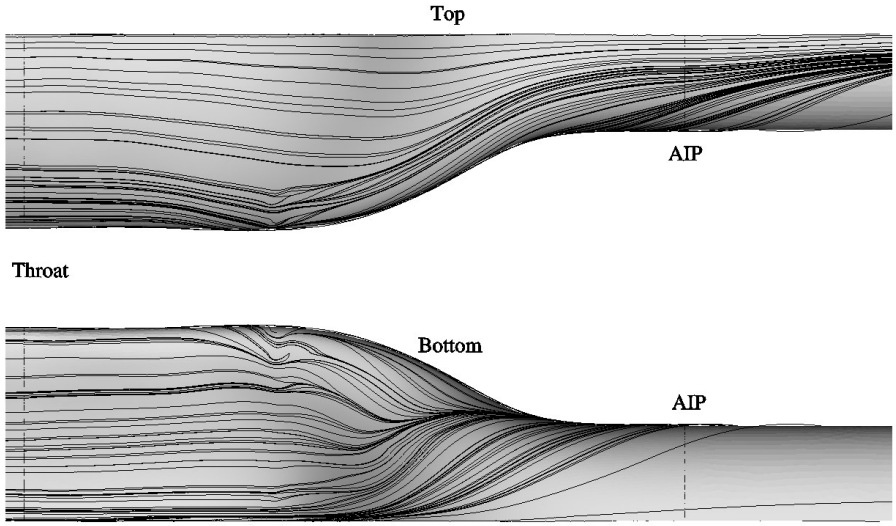

(a) Configuration 3

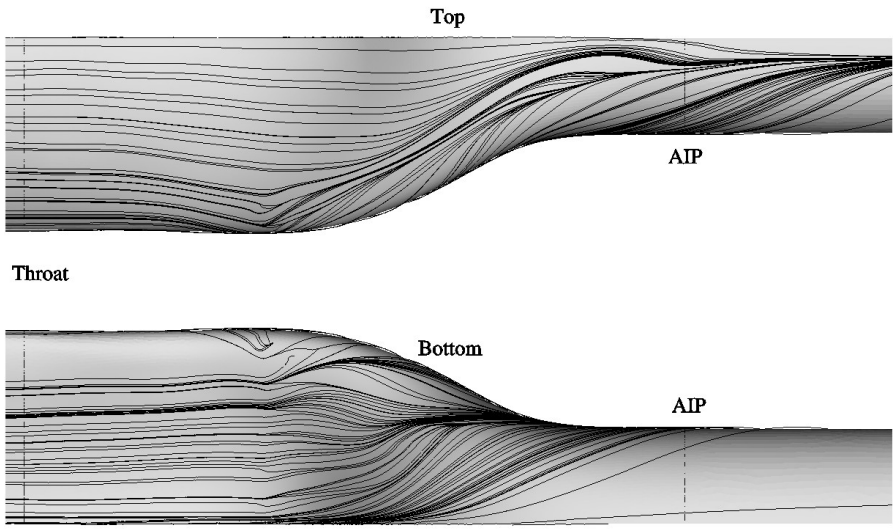

(b) Configuration 8

Figure 41. Comparison of oilflow visualization for configurations 3 and 8

6.3 Results and analysis of the optimization

In this paragraph, the results of the experimental design process are discussed. As mentioned in the introduction to this part on the optimization of the VG configuration, the aim is to minimize the DC60 indicator and maximize the total pressure recovery at the AIP. In this study, only the continuous values of these two quantities are considered for the optimization (using the discrete values instead might lead to somewhat different conclusions).

Figure 42 shows the results of the experimental design following the procedure and notations described in [6]. Each input factor (height, spacing and length) is identified by a letter (A, B and C respectively), their value is either -1, 0 or +1 depending on if it is the lower possible value, the middle one or the higher one. The parameters AB, AC, BC and ABC show the coupling between two or three input parameters. All the results in Figure 42 are obtained for the 15 configurations of the CCF design and each point is an average value of several configurations. Note the very small scale used for the y-axis in Figure 42(b). The analysis reveals that both the height and length are critical parameters that influence the results a lot. The influence of the spacing is lower and there is no strong coupling between any parameter. Both results in Figures 42(a) and 42(b) indicate that low (height = -1) and short (length = -1) VGs are preferable, leading to a small DC60 and a large recovery. The spacing should be large in order to reduce the DC60 but that conclusion is less clear for the total pressure recovery.

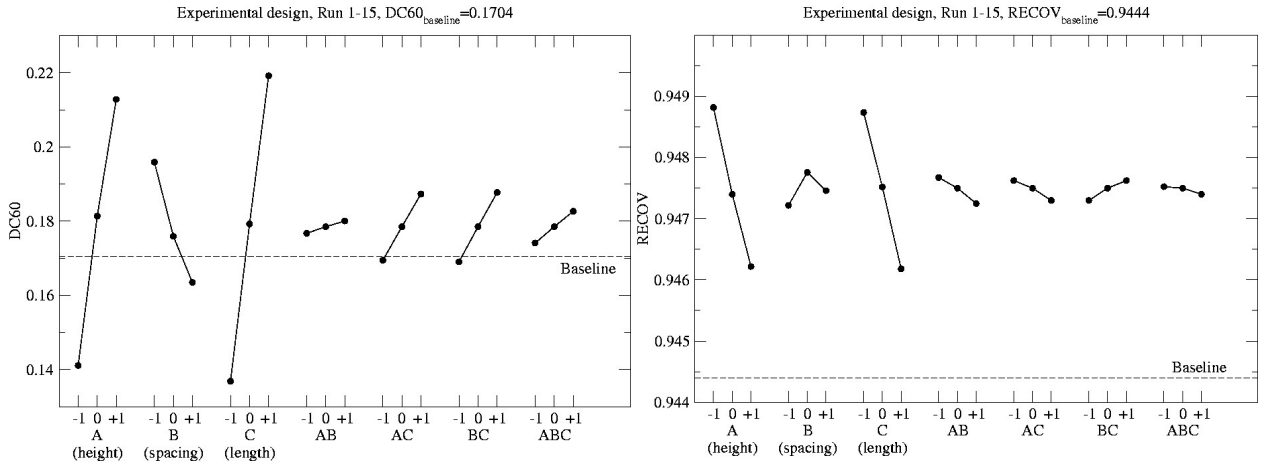

(a) DC60

(b) Total pressure recovery

Figure 42. Results of the experimental design for DC60 and total pressure recovery

The response surfaces of the optimization for the DC60 indicator and the total pressure recovery are shown in Figure 43. Only the 15 configurations of the CCF design are taken into account to build the surfaces (configurations 16 and 17 are shown in Figure 43(a) as separate points). For each quantity, three surfaces are created for the three possible spacings, the black points representing the configurations tested. The analysis is not too difficult because each spacing forms a

nearly flat surface that is almost parallel to the others. The trend for the DC60 is easily identified: shorter and smaller VGs with a large spacing yield a lower DC60 and as the size of the VGs increases so does the DC60. The total pressure recovery shows the same trend (smaller VGs should be preferred) but the effect of the spacing is less clear and in any case the improvements are limited. The optimum identified by the optimization is configuration 3 that yields both the lowest DC60 and the highest total pressure recovery.

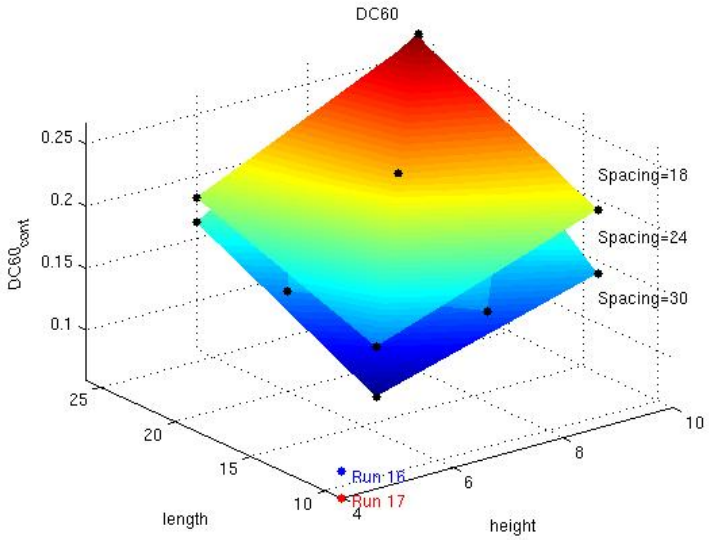

(a) DC60

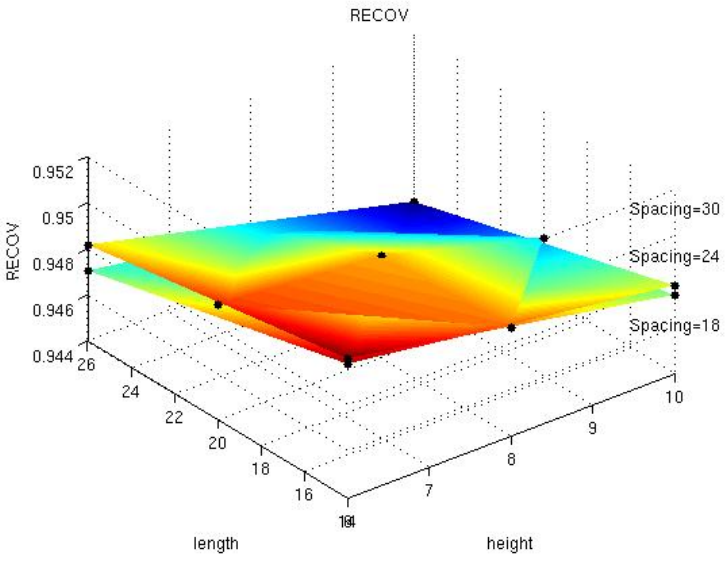

(b) Total pressure recovery

Figure 43. Response surfaces for DC60 and total pressure recovery

6.4 Additional configurations tested

Based on the conclusions of the CCF design, four additional configurations were tested to see if improvements could be made to the already tested 15 configurations. These computations are not actually part of the optimization process but rather tests performed on the side. Two configurations test the influence of the number of VGs (or their circular distribution) and the two others examine VGs with lower height to see if the good performance of small VGs, established in the optimization, can be improved with even smaller VGs.

6.4.1 Influence of the number of VGs

Configuration 3, identified in the CCF design as the optimum configuration, has been used as the baseline case for this part of the study. The two new configurations tested, called 3a and 3b, keep the same VG geometry as configuration 3 (h = 6mm, l = 14mm, s = 30mm) but the number of VGs is different: 14 for configuration 3a and only 10 for configuration 3b. Figure 44 shows how the VGs are placed: by comparison with configuration 3 (Figure 36(a)), configuration 3a (Figure 44(a)) is missing the two VGs on the upper wall and configuration 3b (Figure 44(b)) is, in addition, missing the two VGs close to the symmetry plane. Such VG configurations have been chosen to see how important VGs on the top wall and in the center of the duct are.

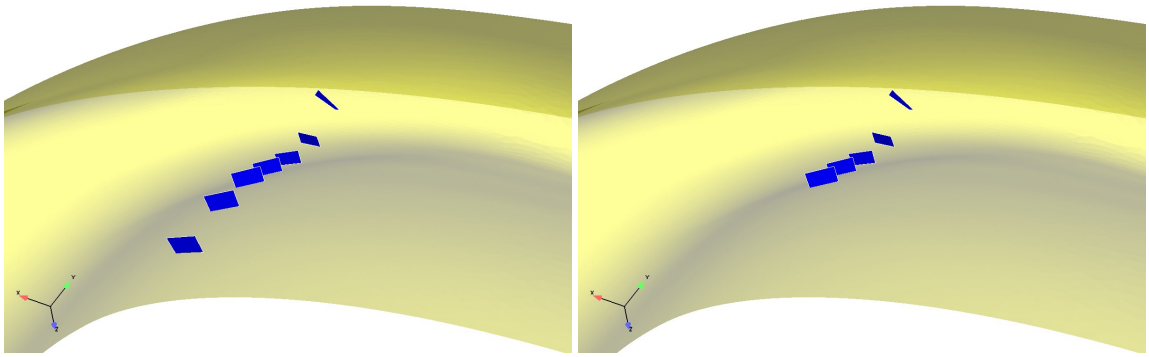

(a) Configuration 3a (b) Configuration 3b

Figure 44. VG geometry: configurations 3a and 3b

The results for these two new configurations indicate a rather low dependence on the number of VGs for the DC60 and total pressure recovery (see Table 3). However by looking at the total pressure contours at the AIP (Figure 45) and the circumferential distribution of $DC60^*$ (Figure 46) some conlusions can be drawn on the positions of the VGs. It is clear that the results for configurations 3a and 3b are very similar which indicates, as expected, that the central VGs are not very important. However their presence slightly improves both the DC60 and the total pressure recovery, especially in the bottom part of the AIP. The main difference in Figure 46 is between configurations 3 and both 3a and 3b. The large difference is at the top of the AIP and is caused by the VGs placed on the top wall of the duct. The vortices created by these two VGs increase the losses at the top of the AIP but make it more uniform (lower and almost constant $DC60^*$).

This study thus indicates that all the VGs in configuration 3 should be included.

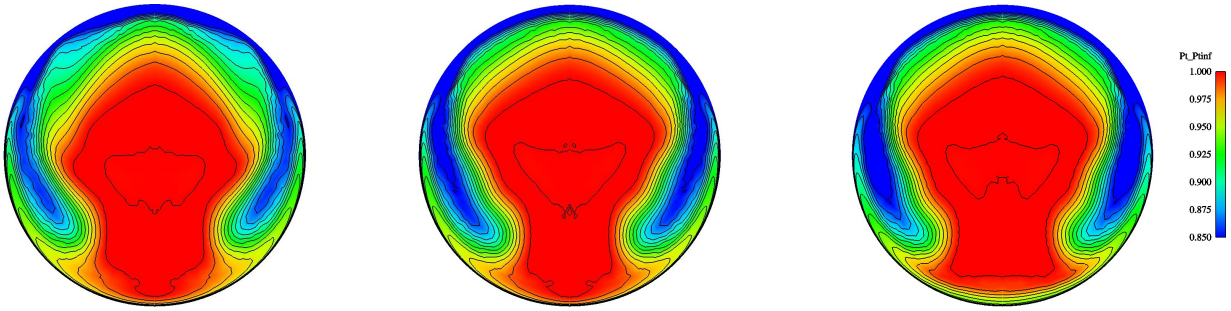

(a) Configuration 3 (b) Configuration 3a (c) Configuration 3b

Figure 45. Contours of total pressure loss at the AIP for configurations 3, 3a, 3b

Figure 46. Comparison of the circumferential distribution of DC60*, configurations 3, 3a, 3b

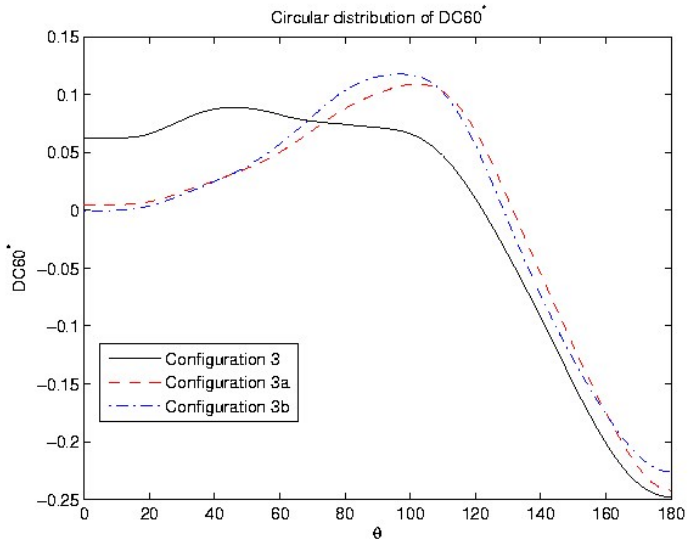

6.4.2 Near sub-layer VGs

In this part, configurations with small VGs are investigated. The height of the VGs chosen for the two configurations (16 and 17) is 4mm i.e. only 50% of the boundary layer thickness, Such VGs are thus at the limit between conventional and sub-layer VGs. The length of the VGs (9mm) has been set in connection with their height to have a ratio l/h close to the one of configuration 3. Configurations 16 and 17 differ by the spacing of the VGs, configuration 16 having the same spacing as configuration 3 and configuration 17 having a relative spacing s/h close to that of configuration 3 (see Table 3 and Figure 47).

The total pressure contours at the AIP in Figure 48 show very similar results for configurations 16 and 17 with pressure losses spread all around the AIP. By looking at the circumferential distribution of DC60* in Figure 49, it becomes clear that the lower DC60 for configuration 17 is achieved through a delay in the

Figure 47. VG geometry for configuration 17

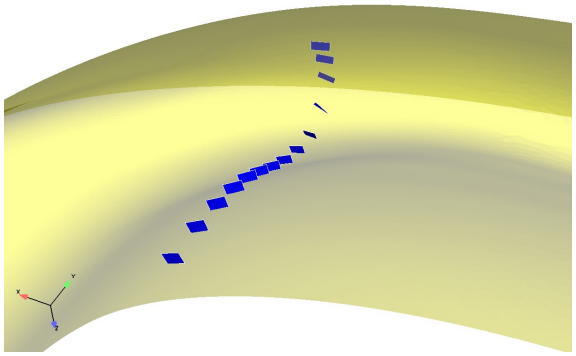

formation of the vortex at around $\theta = 120°$. It is difficult to explain why this happens though.

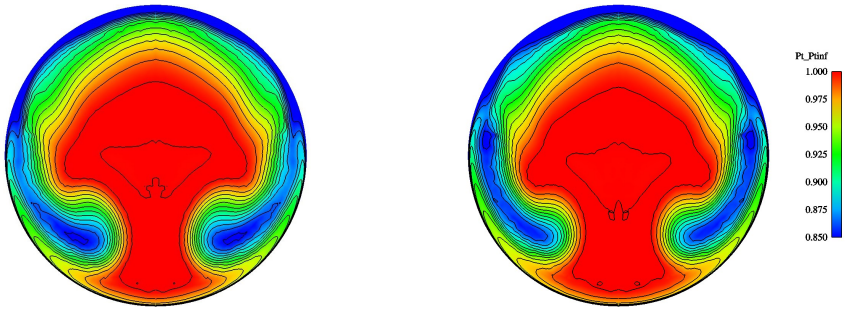

(a) Configuration 16 (b) Configuration 17

Figure 48. Contours of total pressure loss at the AIP for configurations 16 and 17

Figure 49. Comparison of the circumferential distribution of DC60* for configurations 16 and 17

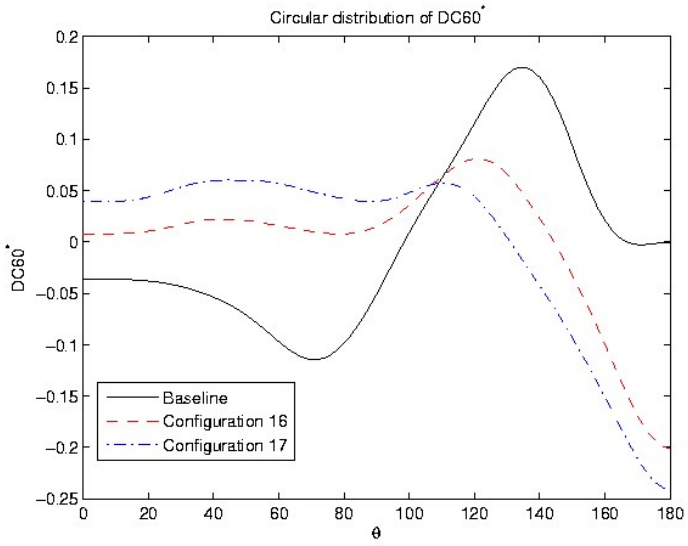

These two configurations show the potential of the smaller VGs to reduce the DC60. Both yield very low distortion independently of the spacing which means that the height (and probably length) is a more important factor than the spacing. By tuning the spacing, better DC60 indicators can maybe obtained. On the other

hand, the total pressure recovery has been better in configurations 3, 3a and 3b so the conclusion does not hold for the recovery.

6.5 Recommendations

In the optimization of the VG configuration presented above, only few parameters have been tested. Many more could be considered and the combinations are endless.

The study shows that the height of the VGs is a very important parameter. If conventional VGs have to be used (h/δ >0.50) then an height of 6mm is recommended and the length should be shorter than 14mm. Surprisingly, these numbers fit with the size of the VGs of the configuration tested in the rig (h = 6mm, l = 10mm) and computed in the first part of the study. However, no real effect of the VGs was noticed then. When comparing the two configurations (Figure 50), it becomes clear that the main difference is not the size of the VGs, nor is it the x-position of the VGs or their spacing but rather their number and the fact that in the experimental configuration, there are no VGs in the outer part of the duct where the separation starts. By simply adding VGs there following the alignment of the VGs already present, improvements would certainly be made. In addition, these VGs in the corner would have a more upstream position which is preferable. Sub-layer VGs have not been investigated in this study. A completely different

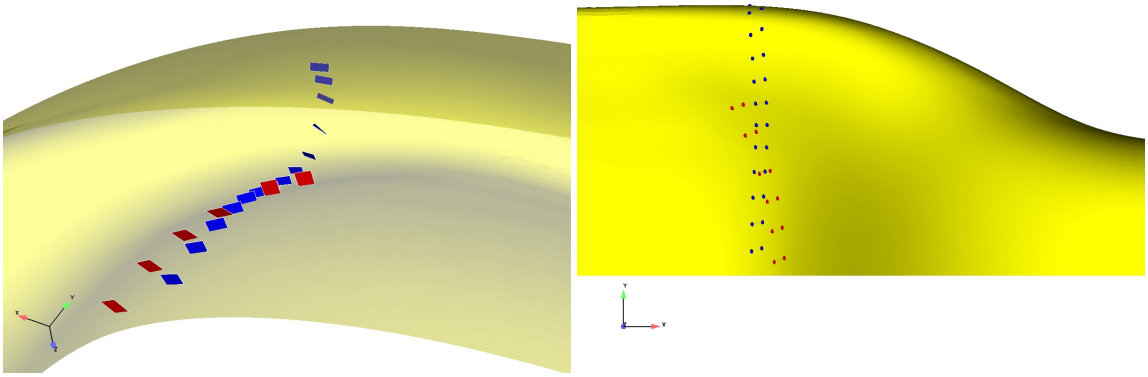

(a) 3D view

(b) Bottom view showing the relative positions of the corners of the VGs

Figure 50. Comparison of VG configurations: rig-test configuration (red), configuration 17 (blue)

parameter setting would be necessary (smaller height with much longer length and a larger number) to run an optimization process. However, the potential of such VGs has been shown (see for example [7]) and they should not be ruled out. In particular, the total pressure recovery might be improved if the pressure losses are restricted to the boundary layer and massive separation limited.

In conclusion of this optimization part, for a future rig test with an improved VG configuration several options are possible: choose configuration 3; test smaller VGs and try configuration 17; modify the experimental configuration by adding

more VGs. One of the two first options is necessary to compare with the CFD results presented above and the third option is hopefully easily set up and worth a try.

7 Sensitivity study

7.1 Turbulence model

All the results presented above were obtained with EDGE using the k-ω Wallin & Johansson EARSM turbulence model. In order to check the dependence of the results on the turbulence model, case 5909 has been run with the standard Wilcox k-ω model [8].
The results at the AIP in Figure 51 compare very well with those obtained with the EARSM model (Figure 11). The double vortex does not seem as developed as with the EARSM model but otherwise the flow picture is the same.

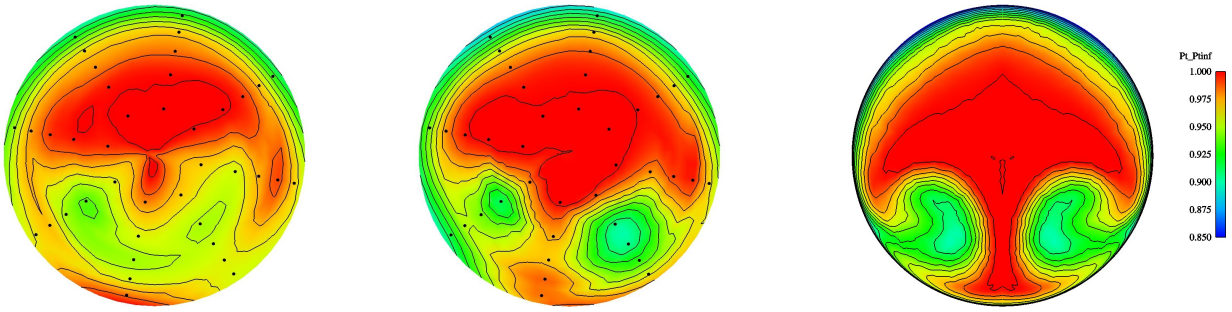

(a) Experiment (b) CFD interpolated (c) CFD

Figure 51. Contours of total pressure loss at the AIP: case 5909, W_{ac}=27.47 kg/s, k-ω turbulence model

The results obtained with the k-ω model are:

- $RECOV_{disc.}$ = 0.9696, $RECOV_{cont.}$ = 0.9675
- $DC60_{disc.}$ = 0.2296, $DC60_{cont.}$ = 0.1559
- D_{rad} = 0.0307

The total pressure recovery does not seem influenced by the turbulence model, only a small difference of 0.2% is noticed. There is a larger difference for the prediction of the DC60 which is improved by 1.5% for the calculation with the continuous method whereas the discrete method gives a worsening of 6.6%.
In Figure 52, the pressure distribution on the wall of the S-duct is compared for both turbulence models with the experimental values. The turbulence modelling has only a very small influence on the pressure distribution and the overall differences with the experimental data remain with the k-ω model.
The oilflow picture in Figure 53 is also very similar to the one with the EARSM model (Figure 29) although the focus is now less clear. The streamlines confirm that the separation takes place at approximately the same location as the one predicted with the EARSM model, which gives more confidence in the results presented above.

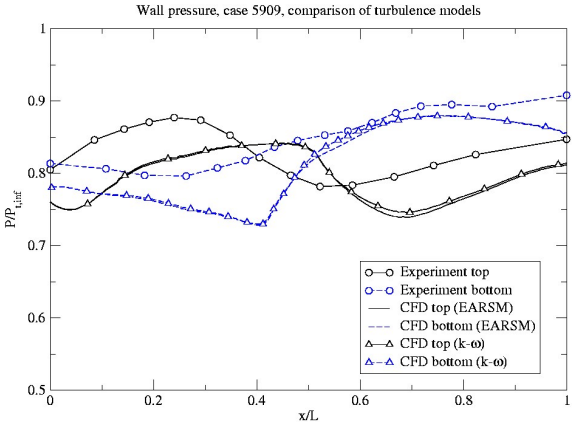

Figure 52. Pressure distribution on the wall: case 5909, k-ω turbulence model

Figure 53. Case 5909 (no VG), k-ω turbulence model

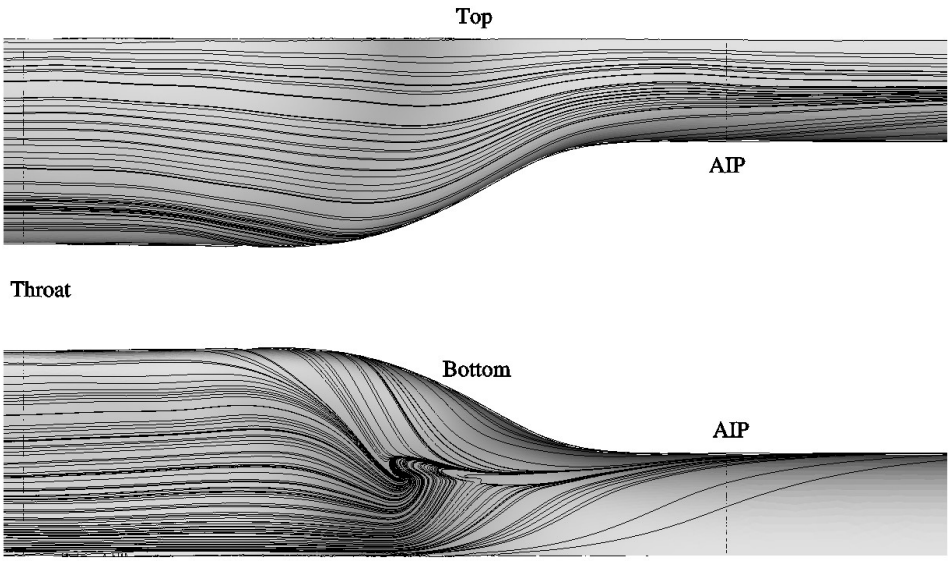

8 Conclusion

In this report, computations of an S-duct with the flow solver EDGE have been presented. In the first part of the study, the results of computations for several mass flow conditions, with or without VGs to control the boundary layer separation, are compared to experimental data obtained in a rig test. In order to easily set the flow conditions, two newly implemented numerical boundary conditions are used at the inlet and outlet of the duct. The VGs are simulated using a VG model, also newly implemented in the flow solver, that makes it easy to change the VG configurations without remeshing. The comparison between the CFD and experimental results is done by looking at the flow at the AIP. The main features of the flow (formation of a system of counter-rotating vortices) are well predicted. The total pressure recovery computed agrees also very well with the experimental data. However, the prediction of the DC60 distortion indicator is rather poor and very sensitive to the method used. The CFD analysis confirms the experimental finding that the VG configuration tested does not improve the quality of the flow at the AIP.

In the second part of the report, the shape and position of the VGs have been optimized to reduce the distortion at the AIP and improve the total pressure recovery. Only conventional VGs have been considered and the optimization is performed on the height, length and spacing of the VGs. The results of the optimization show that small VGs are preferable and a reduction of 65% of the DC60 is achieved. The total pressure recovery is only marginally improved.

Acknowledgements

The author would like to acknowledge all the people involved in this project: Magnus Tormalm (FOI) for the introduction to duct flow, the help with post-processing and his good advice; Anna Svärd and Dag Eriksson (FOI) for the help with the experimental data; Michael Säterskog (Saab AB), the project leader, for answering my questions and guiding the way. A special thanks goes to Adam Jirásek (FOI) who developed and implemented all the new features used in this study and, most of all, explained me how to use them. The beginning was tough but everything finally worked.

References

[1] P. Eliasson. Edge, a Navier-Stokes solver for unstructured grids. In *Proceedings of Finite Volumes for Complex Applications III*, pages 527–534. ISBN 1 9039 9634 1, 2002.

[2] Edge homepage. www.edge.foi.se, last accessed October 11th 2004.

[3] A. Jirasek. Mass flow and mach number boundary conditions for subsonic inflow and outflow. Technical Report FOI-R???-SE, ISSN 1650-1942, FOI, Division of Aeronautics FFA, June 2004 (to appear).

[4] A. Jirasek. A modified vortex generator model and its application to complex aerodynamic flows. Technical Report FOI-R-1204–SE, ISSN 1650-1942, FOI, Division of Aeronautics FFA, March 2004.

[5] S. Wallin and A. Johansson. A complete explicit algebraic reynolds stress model for incompressible and compressible turbulent flows. *Journal of Fluid Mechanics*, 403:89–132, 2000.

[6] S. R. Schmidt and R. G. Launsby. *Understanding industrial designed experiments*. Air Academy Press, 4th edition, ISBN 1-880156-03-2, October 1994.

[7] J. C. Lin. Review of research on low-profile vortex generators to control boundary-layer separation. *Progress in Aerospace Sciences*, 38:389–420, May-July 2002.

[8] D. C. Wilcox. Reassessment of the scale determining equation for advanced turbulence models. *AIAA Journal*, 26(11), 1988.

Issuing organisation
FOI – Swedish Defence Research Agency
Division of Aeronautics, FFA
SE-172 90 STOCKHOLM

Report number, ISRN
FOI-R--1438--SE

Report type
Scientific report

Month year
November 2004

Project number
E830067

Customers code
3. Aeronautical Research

Research area code
7. Vehicles

Sub area code
79. Interdisciplinary Projects regarding Vehicles

Author(s)
Yann Le Moigne

Project manager
Magnus Tormalm

Approved by
Torsten Berglind
Head, Department of Computational Physics

Scientifically and technically responsible
Magnus Tormalm

Report title

NFFP 542 Project report: CFD simulations of an S-duct with conventional vortex generators and comparison with experimental data

Abstract

This report presents CFD simulations of the flow in an S-duct with vortex generators (VGs) added to control the boundary layer separation. The computations are performed with the flow solver EDGE and use is made of two newly implemented boundary conditions and a VG model that makes it possible to investigate several VG configurations without remeshing.

The first part of the report deals with the comparison of experimental data and CFD results for the S-duct at several mass flow conditions, with and without VGs. The comparison is essentially made at the Aerodynamic Interface Plane (AIP) where total pressure contours are compared and the distortion indicator DC60 calculated. Overall good agreement is obtained except for the prediction of the DC60.

In the second part, an optimization of the VG configuration is performed to improve the quality of the flow at the AIP. The optimization procedure is based on the experimental design process followed by an analysis with the response surface method. An improvement of the DC60 index by 65% is achieved while the total pressure recovery remains constant.

Keywords

S-duct, vortex generator, boundary layer control, DC60, total pressure recovery, experimental design, vortex generator model, mass flow boundary condition

Further bibliographic information

ISSN
1650-1942

Pages
59

Language
English

Price
Acc. to price list

Security classification
Open

Utgivare	Rapportnummer, ISRN	Klassificering
Totalförsvarets Forskningsinstitut – FOI Avdelningen för Flygteknik, FFA SE-172 90 STOCKHOLM	FOI-R--1438--SE	Vetenskaplig rapport
	Månad år November 2004	Projektnummer E830067
	Verksamhetsgren 3. Flygteknisk forskning	
	Forskningsområde 7. Farkoster	
	Delområde 79. Breda projekt inom farkoster	
Författare Yann Le Moigne	Projektledare Magnus Tormalm	
	Godkänd av Torsten Berglind Chef, Institutionen för Analys och beräkningar	
	Tekniskt och/eller vetenskapligt ansvarig Magnus Tormalm	

Rapporttitel

NFFP 542 Projektrapport: Strömningsberäkningar av en S-kanal med konventionella virvelgeneratorer och jämförelse med experimentella data

Sammanfattning

Den här rapporten beskriver strömningsberäkningar av en S-kanal med virvelgeneratorer (VG) för att kontrollerar gränskiktsavlösning. Beräkningar gjordes med strömningslösaren EDGE och två nya randvillkorer samt en VG model har använts. Den sistnämnda gör det möjligt att undersöka olika VG konfigurationer utan behov av nya beräkningsnät.

I första delen av rapporten, jämförs experimentella data med resultat från strömningsberäkningar för olika massflöden med och utan VG. Jämförelserna görs vid Aerodynamic Interface Plane (AIP) där totalttrycksfördelning jämförs och distorsionsindex DC60 beräknas. Bra överensstämmelse uppnås för totalttrycksåtervinst men resultat för DC60 är något sämre.

Andra delen av rapporten beskriver en optimering av VG konfigurationen med syfte att förbättra strömningskvalitet vid AIP. Optimeringsprocessen är baserad på en experimentell design metod och resultatanalys på response surface metoden. En förbättring av DC60 med 65% uppnås samtidigt som totalttrycksåtervinsten förblir den samma.

Nyckelord

S-kanal, virvelgenerator, gränsskikt kontroll, DC60, totalt tryck återvinst, experimentell design, virvelgenerator model, massflöde randvillkor

Övriga bibliografiska uppgifter

ISSN	Antal sidor	Språk
1650-1942	59	Engelska
Distribution enligt missiv Distribution	Pris Enligt prislista	
	Sekretess Öppen	